

Glacial isostatic stress shadowing by the Antarctic ice sheet

Erik R. Ivins

Jet Propulsion Laboratory, California Institute of Technology, Pasadena, California, USA

Thomas S. James

Geological Survey of Canada, Sidney, British Columbia, Canada

Volker Klemann

GeoForschungsZentrum Potsdam, Geodesy and Remote Sensing, Telegrafenberg, Potsdam, Germany

Received 1 September 2002; revised 26 March 2003; accepted 31 July 2003; published 12 December 2003.

[1] Numerous examples of fault slip that offset late Quaternary glacial deposits and bedrock polish support the idea that the glacial loading cycle causes earthquakes in the upper crust. A semianalytical scheme is presented for quantifying glacial and postglacial lithospheric fault reactivation using contemporary rock fracture prediction methods. It extends previous studies by considering differential Mogi-von Mises stresses, in addition to those resulting from a Coulomb analysis. The approach utilizes gravitational viscoelastodynamic theory and explores the relationships between ice mass history and regional seismicity and faulting in a segment of East Antarctica containing the great Antarctic Plate (Balleny Island) earthquake of 25 March 1998 (M_w 8.1). Predictions of the failure stress fields within the seismogenic crust are generated for differing assumptions about background stress orientation, mantle viscosity, lithospheric thickness, and possible late Holocene deglaciation for the *D91* Antarctic ice sheet history. Similar stress fracture fields are predicted by Mogi-von Mises and Coulomb theory, thus validating previous rebound Coulomb analysis. A thick lithosphere, of the order of 150–240 km, augments stress shadowing by a late melting (middle-late Holocene) coastal East Antarctic ice complex and could cause present-day earthquakes many hundreds of kilometers seaward of the former Last Glacial Maximum grounding line. *INDEX TERMS:* 7230

Seismology: Seismicity and seismotectonics; 8164 Tectonophysics: Stresses—crust and lithosphere; 1208

Geodesy and Gravity: Crustal movements—intraplate (8110); 1645 Global Change: Solid Earth; 5104

Physical Properties of Rocks: Fracture and flow; *KEYWORDS:* Antarctic Plate Earthquake, Wilkes Basin, neotectonics, Antarctic ice sheet, Coulomb stress, Transantarctic Mountain Ranges

Citation: Ivins, E. R., T. S. James, and V. Klemann, Glacial isostatic stress shadowing by the Antarctic ice sheet, *J. Geophys. Res.*, 108(B12), 2560, doi:10.1029/2002JB002182, 2003.

1. Introduction

[2] A rich and diverse set of observations of glacioisostatic-related faulting now exist that causally relate the last glacial age in Fennoscandia and eastern Canada with the emergence of regional Holocene fault scarps and young offset features [Lagerbäck, 1979, 1992; Adams, 1989; Muir-Wood, 1989; Dehls *et al.*, 2000]. Complementing these observations are studies of regional earthquake focal mechanism and seismicity patterns [Hasegawa, 1988; Arvidsson, 1996; Hicks *et al.*, 2000]. These studies indicate that there exists a geophysically important brittle component of past and present-day postglacial land emergence and deformation [Johnston, 1989; Spada *et al.*, 1991; James and Bent, 1994; Klemann and Wolf, 1998; Wu and Johnston, 2000; Zoback and Grollmund, 2001].

The Antarctic continent has been glacially loaded and unloaded at least since the last interstadial (30–46 kyr BP) [Domack *et al.*, 1991; Zwart *et al.*, 1998; Nakada *et al.*, 2000; Denton and Hughes, 2000], suggesting that ice load related faulting and seismicity may be especially important.

[3] In this paper the principal model elements for the isostatic loading caused by Last Glacial Maximum ice sheet growth and retreat are assembled in order to assess the magnitude, spatial pattern and Earth structure rheology parameter sensitivity of predicted present-day brittle failure in the Antarctic plate. In the present study we focus on the northeastern sector of East Antarctica, from Terre Adelie in Wilkes Land in the west to Victoria Land in the east and from about 78.5°S to 62.5°S, encompassing the continental shelf (see Figure 1). The region has some constraints on deglacial history [Domack *et al.*, 1991; Denton and Hughes, 2000] and some seismic networks have operated during the past decade [Gambino

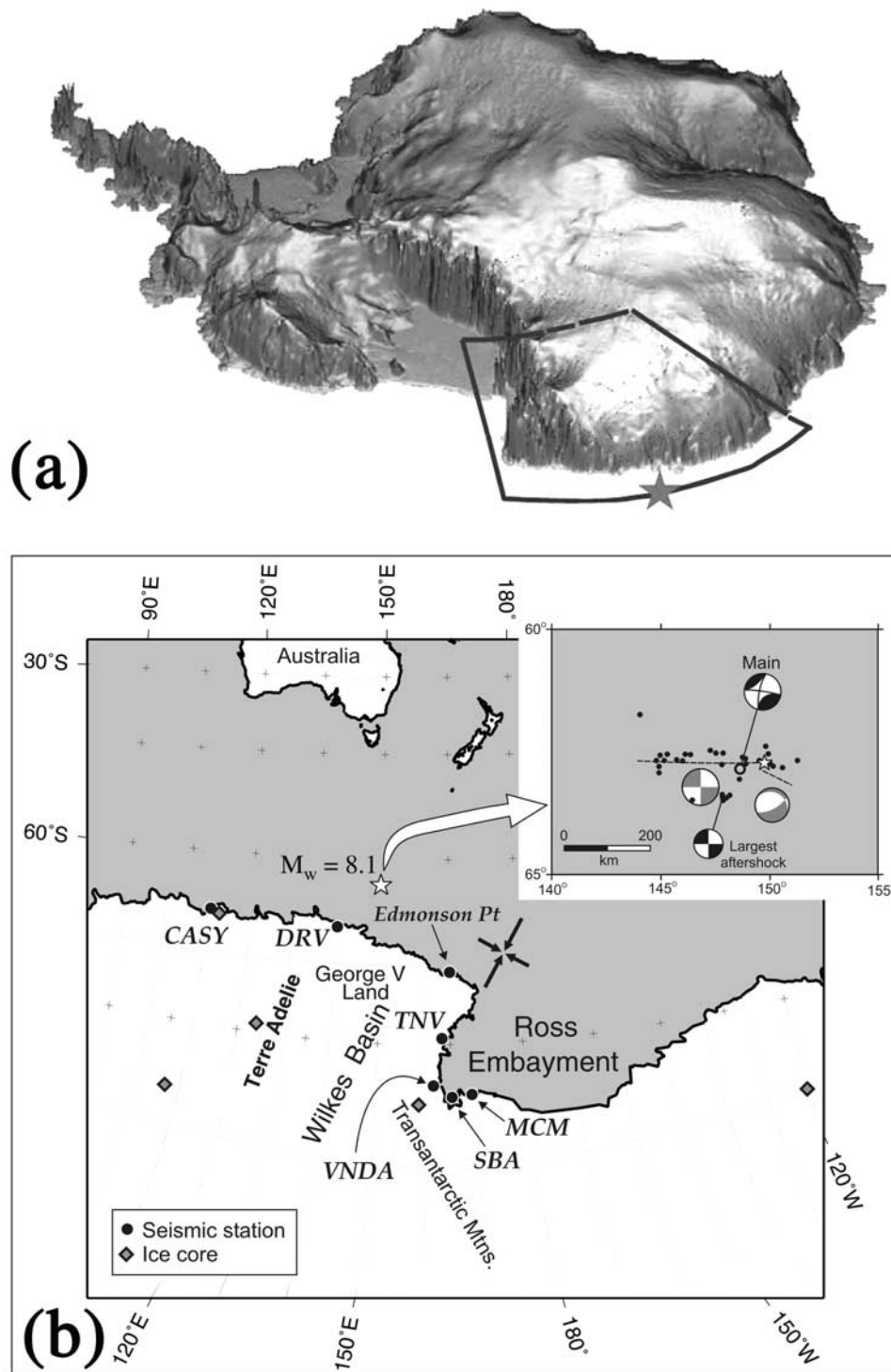


Figure 1. Location maps showing (a) the region of study with a digital elevation map (DEM) and (b) the approximate regional horizontal stress orientation and relative magnitude offshore. The star symbol locates the main Balleny Island earthquake event. Throughout, we refer to the northeast sector of the Antarctic Plate as the area bounded with a solid line in Figure 1a. Permanent seismic stations are TNV, Terra Nova Bay; SBA, Scott Base; Vnda, Vanda; MCM, McMurdo Sound; DRV, Dumont d’Urville; and CASY, Casey Station [see Reading, 2002; Bannister and Kennett, 2002]. Edmonson Point was part of a temporary Italian network described by Gambino and Privitera [1994]. A map of the TransAntarctic Mountains Seismic Experiment arrays is found at <http://www.rps.psu.edu/antarctica/graphics/SPoleMap.jpg>. The DEM in Figure 1a is based on ERS-1 altimeter data <http://www.cpg.mssl.ucl.ac.uk/orgs/cp/html/glac/topog.html>. The orthogonal arrows in Figure 1b show horizontal background stresses suggested by Antolik *et al.* [2000], which are used in the fault stability analysis here. In several numerical experiments the orientation of S_{Hmax} is varied substantially.

and Privitera, 1994; Bannister and Kennett, 2002; Reading, 2002]. In addition, there exists a permanent GEOSCOPE seismic station at the French scientific station at Dumont d'Urville (DRV, 140°E, 67°S) [Roult *et al.*, 1999]. Moreover, it has been suggested that the 25 March 1998 $M_w = 8.1$ Balleny Island earthquake (see Figure 1b), with an epicenter located some 575 km to the north and east of the DRV GEOSCOPE station [Henry *et al.*, 2000], was triggered by glacial isostatic adjustment (GIA) processes [Tsuboi *et al.*, 2000; Kreemer and Holt, 2000].

[4] A simple semianalytical method is employed for predicting the lagged stress response throughout an elastic crust whose tectonic stress field is perturbed by both the glacial surface load and by viscoelastic gravitational flow at depth. In this paper we consider brittle failure in the presence of the GIA-induced stress field with both Coulomb theory [Wu and Hasegawa, 1996a] and with triaxial fracture theory [Mogi, 1971].

[5] Via a series of numerical experiments that use a contemporary deglaciation history for Antarctica, it is predicted that the crust beneath the northeasternmost sector of the East Antarctic ice sheet should contain regions of both enhanced and muted failure stresses relative to ambient, nonglacially forced, conditions. These regions are called stress shadows as they are affected at a level sufficient to cause detectable changes in earthquake occurrence. The terminology borrows from the vernacular popularized in recent studies of aftershocks [Stein, 1999; Hori and Kaneda, 2001]. In these studies an earthquake perturbs the static stress field of adjacent crust. Here it is the evolution of an ice sheet and the solid Earth viscoelastic gravitational adjustment processes that push the crust closer to, or further away from, brittle failure. Where enhancement is predicted, the amplitudes are large, ~ 0.5 – 1.5 MPa, compared to the shadowing caused by $M_w \sim 7$ interplate earthquakes (~ 0.01 – 0.1 MPa). The most complete study of GIA seismicity to date is that of Wu *et al.* [1999] for the Fennoscandian ice sheet. Antarctic deglaciation differs from Fennoscandia in an important way, as it involves more recent ice mass changes.

2. Glacial Isostatic Stresses in the Antarctic Crust: General Background

[6] The study of crustal seismicity across the Antarctic continent has been severely hampered by the lack of regional seismic networks. Nonetheless, data collected during the last several years reveal a plate-wide seismic energy release rate similar to that of continental lithosphere in comparable tectonic settings [Reading, 2002]. General principles of faulting suggest that the added overburden caused by the growth of a great ice sheet nudges the crust toward a seismically “mute” state. Subsequent deglaciation, in contrast, nudges the crust toward a state of increased seismic potential [Muir-Wood, 1989; Johnston, 1989]. Clearly, the process produces a time-dependent seismic potential since the isostatic disequilibrium caused by a shifting surface load is continuously relaxing because of viscous mantle flow underlying the brittle elastic lithosphere. A formal treatment for

seismogenic crust experiencing brittle failure evolution that is driven by GIA stress buildup and release has been lucidly presented by Johnston [1989] and Wu and Hasegawa [1996a]. The theory involves defining the differential Coulomb stress, ΔF_C , which provides the basic diagnostic criteria in monitoring the relative suppression or promotion of brittle failure.

[7] This diagnostic parameter is in wide use today in seismic pattern and prediction analysis [Stein, 1999]. As pointed out by King *et al.* [1994] and Wu and Hasegawa [1996a, 1996b], it is also sensitive to the regional preexisting tectonic stress state. For simulations of Fennoscandian glaciation, Wu *et al.* [1999] show that models with and without this preexisting stress state may differ in magnitude and sign of the predicted diagnostic value of ΔF_C throughout deglaciation and at the present-day (Wu *et al.* [1999] call this parameter $FSM^{(b)}$). The appropriate tectonic stress state in Antarctica is thus both a key issue and a possible limitation to the present endeavor. However, structural, seismological and recent theoretical stress flow numerical information indicate that a tentative tectonic stress regime can be assumed.

[8] An alternative indicator of enhanced shear fracturing that uses all of the principal stress differences may also be employed. In particular, the octahedral shear stress, τ_{oct} , defines a critical threshold parameter [Mogi, 1971]. The failure law employed here is guided by recent fracture experiments for analyses of the KTB drill hole stress data [Chang and Haimson, 2000]. Comparison of the latter to the traditional Coulomb law allows us to examine some of the differences that might arise because of the assumption of different brittle failure criteria.

[9] On interglacial timescales the stress state in the northeastern Antarctic plate resides well below frictional equilibrium (BFE). Stress indicators derived from the Balleny Island earthquake and its aftershocks [Antolik *et al.*, 2000; Henry *et al.*, 2000] may be used to bound the tectonic stress state. This state conforms to the Cenozoic structural patterns in Victoria Land [Wilson, 1999] and is supported by inferences from global plate motion and mantle flow simulations [Steinberger *et al.*, 2001] as well as regional seismic anisotropy studies [Pondrelli and Azzara, 1998]. However, new borehole stress data indicate a tectonic stress orientation [Jarrard *et al.*, 2001] quite different from that inferred from the great intraplate Balleny Island earthquake and this is also given some consideration in the parameter study.

[10] At Last Glacial Maximum earthquakes are suppressed because of the overburden caused by the more massive ice sheet. Subsequent deglaciation moves the crust closer to brittle failure. Unlike Fennoscandia and Laurentia, the ice unloading in Antarctica may be considerably more youthful, by 5000 years or more [Domack *et al.*, 1991; Tushingham and Peltier, 1991; Denton and Hughes, 2000; Nakada *et al.*, 2000; Huybrechts, 2002]. In light of the younger glacial recession, what do gravitational viscoelastic flow models predict for the Antarctic crust today? How sensitive are the predictions to assumptions about the brittle failure criteria and to the tectonic stress state? Could ongoing flexural response of the lithosphere be effectively mapped by observation of present-day seismicity? If so, what is the role of mantle viscosity and lithospheric

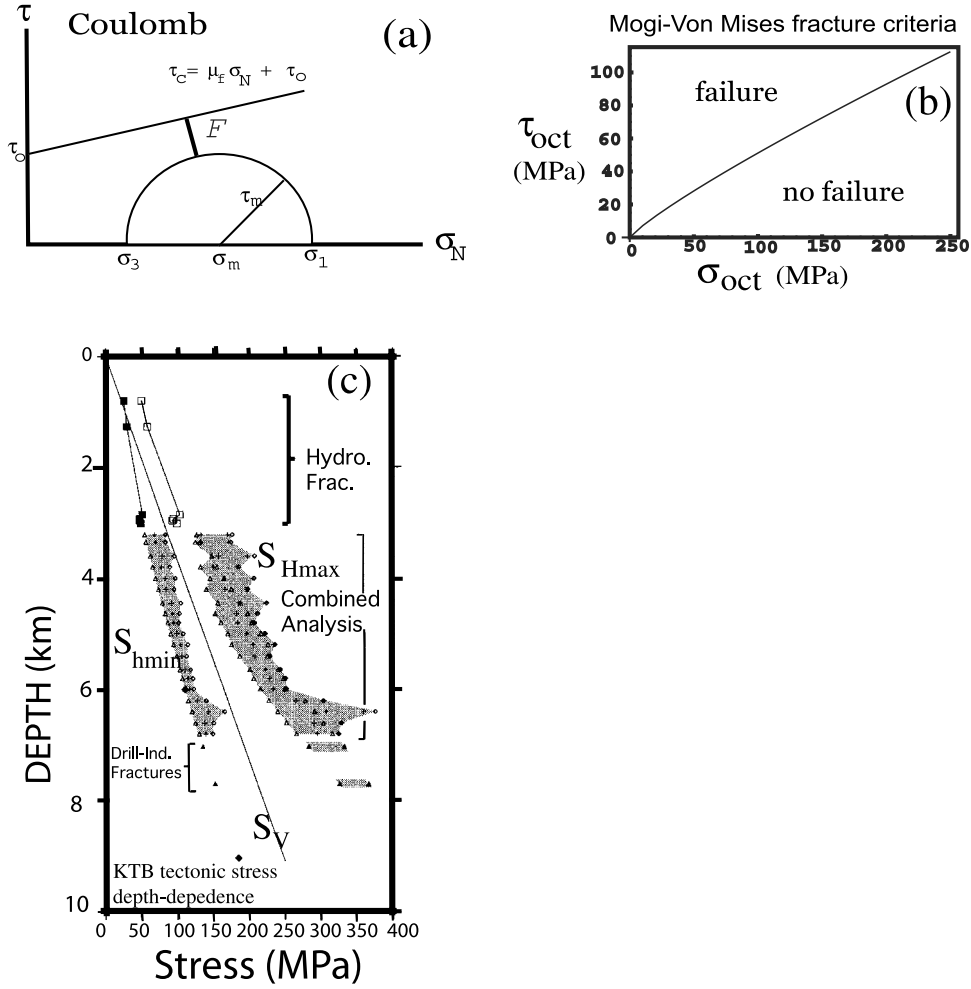


Figure 2. Fracture criteria and horizontal stress depth dependence used in this study. (a) The Coulomb failure theory assumes that shear stress τ and normal stress σ_N act tangential and normal to an optimally oriented fracture surface. (b) For Mogi-von Mises criteria the stability curve in τ_{oct} versus σ_m space is determined experimentally. The relationship shown in Figure 2b is from fracture experiments by *Chang and Haimson* [2000] using 6.36 km depth KTB amphibolite samples. (c) Summary of data that constrain the principal horizontal stress magnitudes to about 9 km depth in the KTB deep drill hole in Bavaria, Germany [adapted from *Brudy et al.*, 1997].

thickness? Answering these questions is the main goal of this paper.

3. Stress Fracture Theory

3.1. Differential Coulomb Approach

[11] The traditional biaxial mechanical theory of faulting predicts that brittle failure occurs when the shear stress, τ , resolved onto a potential plane of fracture, exceeds the value, $\tau_o + \mu_f(\sigma_N - P_p)$, where τ_o is the cohesion (strength at zero confining pressure), σ_N , the resolved normal stress, P_p is the partial pore pressure and μ_f is the coefficient of friction. Prefractured rock has frictional values, generally, in the range: $\mu_f \sim 0.4-0.85$. The differential, $\sigma_N - P_p$, is referred to as the effective normal stress σ_{eff} . However, we can consider σ_1 , σ_2 and σ_3 as the effective principal normal stresses and the development then follows with $\sigma_N = \sigma_{eff}$, without loss of generality [Engelder, 1992]. The biaxial stress state of either isotropically prefractured rock, or of

intact country rock, can be described by the Mohr circle in τ versus σ_N space:

$$\tau^2 + (\sigma_N - \sigma_m)^2 = \tau_m^2 \quad (1)$$

where τ_m and σ_m are the mean shear stress and the mean normal stress, respectively. The maximum (σ_1) and minimum (σ_3) principal stresses are located at the intersection of the circle and the σ_N - axis such that;

$$\tau_m = \frac{\sigma_1 - \sigma_3}{2}, \quad \sigma_m = \frac{\sigma_1 + \sigma_3}{2}. \quad (2)$$

The failure envelope is defined as

$$\tau_c = \mu_f \sigma_N + \tau_o. \quad (3)$$

The geometrical construction of this biaxial failure law is shown in Figure 2a. The minimum stress increase required

to initiate fracturing is shown by the geometrical length F [Johnston, 1989] and at time t_0 is

$$F_0 \equiv (\mu_f \sigma_{m0} + \tau_o) (1 + \mu_f^2)^{-\frac{1}{2}} - \tau_{m0} \quad (4)$$

with the subscript “0” indicating the value at $t = t_0$. Wu and Hasegawa [1996a] assumed a fundamental stress quantity for analyzing the relative stability to earthquake excitation during the GIA deformation process in the lithosphere by comparing some initial stress state, at $t = t_0$, to a stress state later in the evolution at time $t = t_*$. The differential takes the form

$$\Delta F_C \equiv F_* - F_0 = \frac{\mu_f}{\sqrt{1 + \mu_f^2}} \cdot (\sigma_{m*} - \sigma_{m0}) + \tau_{m0} - \tau_{m*}, \quad (5)$$

with subscript “asterisk” now used to indicate the evaluation time t_* . (Wu and Hasegawa [1996a] employ the symbol dFSM for ΔF_C). A stress evolution *diminishing* the probability of brittle fracture corresponds to $\Delta F_C > 0$ and evolution *promoting* failure to $\Delta F_C < 0$.

[12] The Coulomb stress state shown in Figure 2a predicts stability to brittle faulting if the Mohr circle lies below the failure envelope. If the stress state shown in Figure 2a were increased so that the Mohr circle were tangent to the failure envelope, rock would be at the frictional equilibrium (FE) state and failure on an optimally oriented fracture surface is predicted.

3.2. Differential Mogi-Von Mises Stress

[13] The approach adopted by Wu and Hasegawa [1996a] for the Coulomb criterion can be extended to the Mogi-von Mises law which generally accounts for all the principal stress differences and hence can be related to the total deformational strain energy prior to fracture [Mogi, 1971; Brudy et al., 1997]. Toward this purpose, the time evolution of the octahedral shear stress, τ_{oct} , is computed as

$$\tau_{oct} \equiv \left[(\sigma_1 - \sigma_2)^2 + (\sigma_1 - \sigma_3)^2 + (\sigma_2 - \sigma_3)^2 \right]^{\frac{1}{2}} / 3 \quad (6)$$

with the mean stress, σ_m (equation (2)), offering a measure of the normal forces resisting fracture. The Mogi-von Mises failure criterion then takes the form:

$$F_M \equiv \Phi(\sigma_m) - \tau_{oct}. \quad (7)$$

Brittle fracture is predicted for $F_M < 0$ with an empirically based $\Phi(\sigma_m) \approx a\sigma_m^n$. With stress in units of MPa, Chang and Haimson [2000] find for triaxial experiments with amphibolite: $a \approx 1.77$ and $n \approx 0.86$. In Figure 2b the specific law developed experimentally by Chang and Haimson [2000] is shown in dimensional units. The differential Mogi-von Mises stress is

$$\Delta F_M \equiv F_{M*} - F_{M0}, \quad (8)$$

where the subscripts “asterisks” and “0” are the same as in equation (5). Also, the signs of ΔF_M are the same as for ΔF_C . Figure 2a shows a generalized Mohr-Coloumb diagram, while Figure 2b shows the empirical law from Chang and Haimson [2000]. At failure, critical stresses τ_{oct}

and τ_c differ considerably in numerical value. Using the KTB-determined S_{hmin} and S_{Hmax} magnitude as a guide, at $z = 9$ km depth the stress τ_{oct} at failure is ~ 220 MPa, while the shear stress acting at the fracture surface for Coulomb failure is $\tau_c \sim 128$ MPa.

3.3. Tectonic Stress

[14] Within active interplate deformation zones the crust may reside close to the failure condition [Hill, 1982; Morein et al., 1997]. Hence, in the absence of GIA processes and in a crust at frictional equilibrium: $F_0 \rightarrow +0$ and $\Delta F \approx F_*$, where the subscripting on F is removed, generalizing to both failure laws. This assumption might be realistic if significant rates of Quaternary intraplate tectonic activity could be demonstrated.

[15] For the northeastern Antarctic continent, however, geomorphologic constraints derived from cosmogenically dated surface units [Summerfield et al., 1999] in southern Victoria Land indicate a slow rate of landscape evolution over the last 15 Ma. Averaged over that time span, the uplift rate for the Royal Society Range in southern Victoria Land inferred by Sugden et al. [1999] is a mere $8.5 \mu\text{m/yr}$. Relative tectonic quiescence remains controversial, especially near the Transantarctic Mountain escarpment [Wilson, 1999; Dalziel and Lawver, 2001]. However, given the repeat time of major earthquakes within continental plates ($10^3 - 10^5$ years) and the implied slowly varying tectonic stresses [Kanamori and Brodsky, 2001], our stability analysis proceeds by assuming a non-GIA initial tectonic state in which a finite stress has to be supplied to the crust in order to reach the point of shear failure. This is called the below frictional equilibrium (BFE) state.

[16] In a tectonic reference state that has one principal stress aligned with the vertical direction, we can further develop some aspects of the differential Coulomb stress concept, provided that the GIA induced perturbations, σ_1^{GIA} , σ_2^{GIA} and σ_3^{GIA} , are aligned with the background tectonic set of principal directions. The latter is an unlikely scenario. Nonetheless, use of this assumption illuminates the role of the perturbed stress field with respect to GIA-influenced brittle fracture potential. For this tutorial example, a stress state like that of Heim’s Rule is assumed, wherein one of the tectonic horizontal stresses (with principal stresses, $\sigma_1^{(0)}$, $\sigma_2^{(0)}$ and $\sigma_3^{(0)}$) is near the lithostatic value. For a tectonic stress field that drives extensional faulting,

$$\begin{aligned} S_V &= \sigma_1^{(0)} \\ S_{Hmax} &= \sigma_2^{(0)} \\ S_{hmin} &= \sigma_3^{(0)} = S_r \sigma_1^{(0)}, \end{aligned} \quad (9)$$

with S_V , S_{Hmax} , S_{hmin} the vertical, maximum and minimum horizontal principal stresses, respectively, and S_r is the ratio of minimum to lithostatic stress. A background stress favoring strike slip is also considered;

$$\begin{aligned} S_{Hmax} &= (1 + S'_r) S_V = \sigma_1^{(0)} \\ S_V &= \sigma_2^{(0)} \\ S_{hmin} &= \sigma_3^{(0)}, \end{aligned} \quad (10)$$

[Hill, 1982] and, generally, observations support $0 < S'_r < 1$. The driving tractions may be associated with plate motions [Zoback *et al.*, 1989; Ivins *et al.*, 1990]. For comparison, the tectonic states, equations (9) and (10), correspond to the cases of $\zeta < 1$, $\zeta > 1$, respectively, of *Wu and Hasegawa* [1996a, 1996b] ($\zeta \equiv S_{Hmax}/S_V$) and coincide with triaxial extension and compression, respectively. Again for the purpose of elucidation, in the unlikely circumstance that the background and GIA principal directions coincide and $F_0 \rightarrow 0$;

$$\Delta F_C = -\frac{\sigma_1^{GIA}}{2} \left(1 - \mu_f / \sqrt{\mu_f^2 + 1}\right) + \frac{\sigma_3^{GIA}}{2} \left(1 + \mu_f / \sqrt{\mu_f^2 + 1}\right), \quad (11)$$

independent of the preference of stress state for faulting styles, equation (9) or (10). Equation (11) reveals the tendency of the GIA-induced state to promote seismicity. For positive principal stresses it is seen that a state promoting seismicity ($\Delta F_C < 0$) is easily generated. An exception ($\Delta F_C \geq 0$) is, according to equation (11), when

$$\sigma_3^{GIA} < \frac{-\mu_f + \sqrt{1 + \mu_f^2}}{\mu_f + \sqrt{1 + \mu_f^2}} \cdot \sigma_1^{GIA} \quad (12)$$

and with $\mu_f \approx 0.4$ or 0.7 this requires $\sigma_3^{GIA}/\sigma_1^{GIA} < 0.46$ or < 0.27 , respectively. This type of a stress state may, however, occur when the ice overburden promotes a large vertical principal stress and simultaneously a small (dominantly tensional) minimum stress, a situation which should occur directly beneath the ice load [Johnston, 1989]. *Wu and Hasegawa* [1996a] have shown, via numerical computation, that such a stress state, $\Delta F_C \geq 0$, is predicted near the loading center during the ice growth phase. Example equation (11) is illustrative only, and cannot be employed to compute ΔF_M or ΔF_C , as the full tensor nature of the tectonic and GIA stress fields must be taken into account.

3.4. GIA Stress Perturbation With Tectonics

[17] With knowledge of both the orientation and the magnitude of the tectonic components, $\sigma_1^{(0)}$ and $\sigma_3^{(0)}$, for the Antarctic lithosphere it is straightforward to proceed with a failure analysis similar to that used by *Wu and Hasegawa* [1996a] and *Wu et al.* [1999] for studying Laurentide and Fennoscandian GIA earthquake-related deformation processes. For Antarctica, however, the regional field must be estimated using far fewer stress indicators than are available in Canada or Scandinavia.

3.4.1. Neogene Tectonic Regime

[18] Currently, only minimal in situ stress data exist that constrain the Neogene tectonic principal stresses and orientation in Antarctica. There is, however, a limited portion of Victoria Land where fault planes and striae mark a regional Tertiary age transtensional phase [Wilson, 1995; Salvini *et al.*, 1997] and where both dextral and sinistral transfer faults join an extensional rift system in the Ross Embayment. Structural analysis by *Wilson* [1999] indicates that late Cenozoic tectonics involves the combination of a linearly oriented Neogene volcanic system (the Erebus Volcanic Province), contemporaneous sinistral transfer faults (of

W-NW orientation) and a system of N-NE oriented normal faults. These structures could be associated with a tectonic stress field that has S_{hmin} oriented roughly $N35^\circ W \pm 40^\circ$ [also see *Jones*, 1996, Figure 9d]. This regional direction of maximum horizontal stress is roughly consistent with recent numerical plate motion and mantle flow simulations which predict global lithospheric stress patterns [Steinberger *et al.*, 2001]. A shear wave splitting study in Victoria Land by *Pondrelli and Azzara* [1998] identified the fast polarization direction along a WNW-ESE axis, implying a regional S_{hmin} axis at $N14^\circ W$ – $N49^\circ W$.

[19] Recent borehole breakout data obtained by *Jarrard et al.* [2001] indicate quite different principal stress directions, however, in the western Ross Sea. The orientation of S_{hmin} determined at the drill site is $N70^\circ E \pm 5^\circ$ and this could be consistent with dextral strike slip on crustal features such as the David Glacier lineament [Van der Wateren and Cloetingh, 1999; Jarrard *et al.*, 2001] for which there is preliminary evidence of current seismic activity [Bannister and Kennett, 2002].

[20] In sum, current interpretations of the regional tectonic stress are preliminary because of the limited extent of exposed structural outcrop, the limited seismic polarization data, the lack of focal mechanism constraints, the relative lack of timing constraints and the role played by inherited crustal weaknesses [Wilson, 1995, 1999; Jones, 1996].

3.4.2. The 1998 Balleny Island Earthquake and Possible Stress Indicators

[21] The 25 March 1998 Balleny Island earthquake (M_w 8.1, centroid depth of 9–12 km) has a compound rupture mechanism [Kuge *et al.*, 1999; Antolik *et al.*, 2000; Henry *et al.*, 2000]. Analyses by *Kuge et al.* [1999] and *Antolik et al.* [2000] suggest left lateral strike slip and normal faulting subevents. In contrast, a P and SH body wave study by *Henry et al.* [2000] indicated that the first subevent involved left lateral strike slip and that a second subevent was triggered dynamically. The relative horizontal displacements are consistent with GPS-derived relative crustal motion vectors between the Antarctic and Australian plates found by *Dietrich et al.* [2001] using data prior to the M_w 8.1 event.

[22] While such information aids in characterizing the background stress in this portion of the Antarctic plate (see Figure 1), to the south and west the indicators differ. The borehole breakout data [Jarrard *et al.*, 2001] and the orientation of rifting in the Adare Trough [Candie *et al.*, 2000] suggest a NE-SW tensional and NW-SE compressional stress regime. Although stress orientations are difficult to decipher from the complex structural overprinting in Victoria Land [Storti *et al.*, 2001], the coexistence of normal and strike slip faulting is compelling throughout the northeastern sector of the Antarctic plate, consistent with $S_{Hmax} \approx S_V$. Using this approximation, equations (9) and (10) are then

$$S_{Hmax} \approx S_V = \sigma_1^{(0)} \approx \sigma_2^{(0)} \quad (13)$$

$$S_{hmin} = \sigma_3^{(0)}$$

with $S'_r \approx 0$ assumed. The background field defined by equation (13) accounts for the main influence of tectonic stress on the crustal fault stability in the presence of ice

sheet change and rebound. The modeled depth variation of the three principal tectonic stresses is assumed to follow the KTB-derived dependence found by *Brudy et al.* [1997] as shown in Figure 2c. As noted above, there is much greater uncertainty about the present-day tectonic field here than in either Scandinavia or eastern Canada.

3.4.3. Tectonic Stress With GIA Perturbation

[23] Stresses associated with GIA processes may be calculated from solutions to the material incremental momentum balance equations

$$\nabla \cdot \underline{\tau} + \rho g \nabla (\mathbf{u} \cdot \hat{\mathbf{k}}) = 0 \quad (14)$$

[*Wolf*, 1985, 2002; *Wu and Hasegawa*, 1996a; *Ivins and James*, 1999] with the constitutive assumption of a Maxwell viscoelastic material. In equation (14), τ is the perturbed material incremental stress tensor associated with a GIA-induced deviation from a lithostatic stress state, \mathbf{u} is the Lagrangian displacement field, g the gravity and $\hat{\mathbf{k}}$ is the unit vector aligned with the downward gravitational force. For a two-layer incompressible Earth model the complete Hankel transformed solution may be obtained analytically, including all components of τ . In equation (14) a pressure giving positive dilatation is also taken to be positive. With this change accounted for, and changes in coordinate systems, the GIA stresses in the elastic layer may be calculated as the stress tensor σ^{GIA} . The unperturbed pressure field (of sign convention opposite to that of tectonic fracture theory) included the material incremental equations of motion (equation (14)) is of the form

$$P^{(0)} = -\rho g z, \quad (15)$$

where z is the depth. It is through this isotropic initial pressure field, $P^{(0)}$, that a displaced material particle is advected into a differing stress environment. The advection of prestress in equation (14) then does not include nonisotropic influences which is consistent with the assumption that there are no horizontal gradients in the background tectonic stress field.

[24] The general strategy assumes that none of the GIA principal stress directions are aligned with the vertical. However, it is determined computationally that the misalignment is small, generally less than 5° and often less than 1° . In the BFE stress state, the sum $\sigma^{\text{GIA}} + \sigma^{(0)}$ is computed, where $\sigma^{(0)}$ is the tectonic background stress tensor transformed [*Jaeger*, 1969, pp. 6–7] into the coordinate frame of the tensor, σ^{GIA} . The latter is computed from the initial value/boundary value problem (equation (14)). For the BFE state and tectonic stress field (equation (13)), the differential Coulomb stress is calculated using equation (5). Relevant fracture parameters are summarized in Table 1.

4. GIA Stress Theory

[25] Using the formal approach of *Wolf* [1985], *Ivins and James* [1999] (hereinafter referred to as IJ99) derived an analytical solution for the vertical surface displacement, $\hat{w}_0(k, s, 0)$, from the four coupled ordinary

Table 1. Scalar Stress Fracture Parameters

Quantity	Definition
<i>Differential Coulomb</i>	
σ_{eff}	effective stress normal to fracture surface
τ_m	mean shear stress
σ_m	mean normal stress
τ_c	critical shear stress at fracture surface
F_0, F^*	minimum stress increase required to reach τ_c
ΔF_C	difference of stress increments F_0 and F^*
μ_f	coefficient of friction
<i>Differential Mogi-von Mises</i>	
τ_{oct}	octahedral shear stress
$\Phi(\sigma_m)$	empirical function defining critical failure envelope
F_M	increment of τ_{oct} required to reach failure envelope
ΔF_M	increment difference between * and 0 stress states
a	scale constant for empirical function $\Phi(\sigma_m)$
n	exponent of σ_m in empirical function $\Phi(\sigma_m)$

differential equations which follow from equation (14). The same four equations (noting a typographical error corrected to $-\rho g k \hat{w}_0$ from $-\rho g \hat{w}_0$, therein), may be employed to derive a more general analytic solution. These include the z dependence for each of four dependent variables that naturally emerge from equation (14). These solutions can then be used to construct the complete time-dependent stress and strain fields within the elastic lithosphere. In the section that follows these analytic solutions are given complete description. The constants appearing in the pair of decay times are given by IJ99.

4.1. Viscoelastic Solutions in Hankel and Laplace Transform Space

[26] The solutions of equation (14) assume an elastic layer over an incompressible Maxwell viscoelastic half space. Within the elastic (top) layer of constant density, ρ_1 , rigidity, μ_1^e , and thickness, h , the Hankel transformed nondimensional solutions for the cylindrical stress components, τ_{zz} and τ_{rz} , are

$$\begin{aligned} \hat{\tau}_{zz0}(k, z, t) = & -e^{-kz} \cdot \{ (1 + kz) \hat{q}_0(k, s; t) \\ & + [(1 - e^{2kz}) \phi_1 + 4k^2 z R_\mu] \hat{A}_1(k, s; t) \\ & + \phi_1 [(1 + kz) - (1 - kz) e^{2kz}] \hat{C}_1(k, s; t) \} \end{aligned} \quad (16a)$$

$$\begin{aligned} \hat{\tau}_{rz1}(k, z, t) = & -\frac{2ke^{-kz}}{\chi_1} R_\mu \{ kz \hat{q}_0(k, s; t) \\ & + [4k^2 z R_\mu - \chi_1 (1 - e^{2kz})] \hat{A}_1(k, s; t) \\ & + kz [\phi_1 - \chi_1 e^{2kz}] \hat{C}_1(k, s; t) \} \end{aligned} \quad (16b)$$

where $\hat{\cdot}_0$ and $\hat{\cdot}_1$ indicate the zeroth and first-order Hankel transforms of wave number, k , respectively, and R_μ is the ratio of lithosphere to mantle rigidity, μ_1^e/μ_2^e . Additional ratios, $R_\delta \equiv gh\delta\rho/\mu_2^e$ and $R_g \equiv \rho_1 gh/\mu_2^e$, and the modified dimensionless wave numbers are;

$$\chi_1 \equiv 2kR_\mu + R_g, \quad \phi_1 \equiv 2kR_\mu - R_g,$$

where $\delta\rho \equiv \rho_2 - \rho_1$. Throughout this section, variables that are dimensionless are assumed, as in Table 2, except with

Table 2. Nondimensionalization (Section 4.1)

Variable	Definition
τ'	τ/μ_2^s
r', z'	$h^{-1}r, h^{-1}z$
\mathbf{u}'	$h^{-1}\mathbf{u}$
s'	$(\eta/\mu_2^s)s$
k'	hk
\hat{w}_0', \hat{u}_1'	$h^{-3}\hat{w}_0, \hat{u}_1$

the primes dropped. The order ν Hankel transform is defined by the operator;

$$\hat{f}_\nu(k) \equiv \mathbf{H}_\nu[F(r); k] \equiv \int_0^\infty rF(r)J_\nu(kr) dr \quad (17a)$$

with inverse operator

$$F(r) \equiv \mathbf{H}_\nu^{-1}[\hat{f}_\nu(k); r] \equiv \int_0^\infty k\hat{f}_\nu(k)J_\nu(kr) dk \quad (17b)$$

where the operator notation \mathbf{H}_ν follows that of *Sneddon* [1972]. The notation $(\cdot \tilde{\cdot})$ indicates the inverse Laplace transform operator that transform the load parameter q_0 and solution parameters A_1 and C_1 from Laplace transform variable, s , to model time, t . The subscripts “1” refer to the layer number “1” or elastic lithosphere. Continuity conditions at the interface between layers 1 and 2 (lithosphere and mantle half space) and surface stress conditions on τ_{rz} and τ_{zz} may be applied to construct the complete solution for A_1 and C_1 . (For additional details, see IJ99, equations 18a, 18b, 22a, 22b, 22c, and 22d). In the Laplace and Hankel transform domain:

$$\begin{aligned} \hat{A}_1(k, s) = & \hat{Q}(k, s) \cdot 2e^{2k} \{ R_\mu [2k^2 R_\mu + R_\delta] \\ & + [4k^2 R_\mu^2 - R_\delta (2R_\mu + k)] \cdot s \\ & - [2k^2 (1 - R_\mu^2) + R_\delta (k + R_\mu)] \cdot s^2 \} \end{aligned} \quad (18a)$$

and

$$\begin{aligned} \hat{C}_1(k, s) = & \hat{Q}(k, s) \{ R_\mu \{ -2kR_\mu [1 - (1 + 2k)e^{2k}] + R_\delta (1 - e^{2k}) \} \\ & + 2R_\mu [2k(1 - R_\mu) - [1 + (1 + 2k)e^{2k}]R_\delta / (2R_\mu) \\ & + R_\delta (1 - e^{2k}) + 2kR_\mu (1 + 2k)e^{2k}] \cdot s \\ & - \{ 2k [1 + (1 + 2k)e^{2k}] - 4kR_\mu + R_\delta [1 + (1 + 2k)e^{2k}] \\ & + 2kR_\mu^2 [1 - (1 + 2k)e^{2k}] \} \cdot s^2 \} \end{aligned} \quad (18b)$$

with

$$\hat{Q}(k, s) \equiv \frac{\hat{q}_0(k, s)}{\hat{\beta}(s^2 + b_1 s + b_0)}$$

and with $\hat{\beta}$, b_0 and b_1 given in Tables 1 and 2 of IJ99. The parameters $\hat{\beta}$, b_0 and b_1 are the sole contributors to the decay spectra governing the viscoelastic relaxation in the half space (layer 2). Together with $\hat{q}_0(k, s)$, all of the remaining terms on the RHS of equations (18a) and (18b) (forming the coefficients of s in the numerator) determine the amplitude factors for the complete solutions.

[27] The assumed axial symmetry about the z axis renders the elastic gravitational boundary value problem at hand a two-dimensional one. Hence only four of the six components of the symmetric stress tensor, τ , need to be considered in polar cylindrical coordinates. For an incompressible lithosphere the two additional incremental stresses are:

$$\begin{aligned} \tau_{\theta\theta}(r, z, t) & \equiv -p + R_\mu \{ \mathbf{H}_0^{-1}[k\hat{u}_1] \pm \mathbf{H}_2^{-1}[k\hat{u}_1] \} \\ \tau_{rr}(r, z, t) & \end{aligned} \quad (19a)$$

with the pressure field [*Klemann and Wolf*, 1998]

$$-p(r, z, t) = 2R_\mu \mathbf{H}_0^{-1}[k\hat{u}_1 + \hat{\tau}_{zz0}], \quad (19b)$$

where $\hat{u}_1(k, z, t)$ is the transformed radial displacement component [*Sneddon*, 1972, p. 349]. Using the methods outlined by *Wolf* [1985] and IJ99, it is straightforward to show that

$$\begin{aligned} \hat{u}_1(k, z, t) = & \left\{ \frac{4k^2 z R_\mu}{\chi_1} e^{-kz} - e^{kz} - e^{-kz} \right\} \cdot \hat{A}_1(k, t) \\ & + kz \left\{ \frac{\phi_1}{\chi_1} e^{-kz} + e^{kz} \right\} \cdot \hat{C}_1(k, t) + \frac{kze^{-kz}}{\chi_1} \cdot \hat{q}_0(k, t). \end{aligned} \quad (20)$$

The Laplace transform inversions, \mathbf{L}^{-1} , are analytic and are given in equations (28)–(33) of IJ99. For example,

$$\hat{A}_1(k, t) = \mathbf{L}^{-1} \tilde{A}_1(k, s) = \sum_{j=1}^J \tilde{A}_j(k, t), \quad (21a)$$

$$\hat{C}_1(k, t) = \mathbf{L}^{-1} \tilde{C}_1(k, s) = \sum_{j=1}^J \tilde{C}_j(k, t), \quad (21b)$$

$$\hat{q}_0(k, t) = \mathbf{L}^{-1} \hat{q}_0(k, s) = \hat{q}_0^*(k) \hat{q}_0^{**}(t), \quad (21c)$$

wherein we let the surface load part \hat{q}_0^{**} be approximated as piecewise continuous with J linear segments

$$\hat{q}_{0j}^{**} = \bar{m}_j t + \bar{b}_j \quad (21d)$$

with \bar{m}_j and \bar{b}_j the slope and y intercept of each of the J piecewise linear segments. For example, in evaluating the stress at time, t , for rebound wherein surface load changes are past events, $\mathbf{L}^{-1} \hat{q}_0(k, s) = 0$, whereas the inversions, $\mathbf{L}^{-1} \tilde{A}_1(k, s)$ and $\mathbf{L}^{-1} \tilde{C}_1(k, s)$ are finite, involving convolutions with \hat{q}_0 . If the glacial load changes at the present-day, the last term on the RHS of

$$\hat{q}_0(k, t) = (\bar{m}_j t + \bar{b}_j) \cdot \hat{q}_0^*(k), \quad (21e)$$

with $\hat{q}_0^*(k)$ given by IJ99 equation (34) for both square-edged and ellipsoidal cross-section disks. To recover the full

deformation field it is important to include the z dependence of the vertical displacement:

$$\hat{w}_0(k, z, t) = -\frac{e^{-kz}}{\chi_1} \left\{ (1 + kz)\hat{q}_0 + [\phi_1 + \chi_1 e^{2kz} + 4k^2 z R_\mu] \hat{A}_1 + [(1 + kz)\phi_1 + (1 - kz)\chi_1 e^{2kz}] \hat{C}_1 \right\}. \quad (22)$$

It is assumed that a downwardly directed z motion is, by convention, negative. Consequently, a minus sign is included on the RHS of equation (22).

4.2. Disk Profiles and Time-Dependent Elastic Layer Solutions

[28] The evolving GIA stress field in the elastic surface layer will be dominated by the stress directly imparted by the ice load during glacial waxing and waning, and indirectly during much of the postglacial phase when the fading viscoelastic memory dominates the deformation. The stress interaction at the glacial-crustal interface is assumed to be entirely elastic, with the ice sheet imparting only a normal traction to the solid crust. The precise form of the forward Hankel transform of the zz component of the interaction depends on the cross-sectional profile of the axisymmetric surface load. All of the axisymmetric load shapes tabulated by *Thoma and Wolf* [1999] were employed for testing the shape dependence of the stress solutions for this study.

4.2.1. Elastic Layer Solution With Inviscid Half Space

[29] By assuming that the half space is an inviscid fluid the dimensional boundary conditions for the elastic layer simplify to $\hat{\tau}_{zz0}^\Delta(h) = -\delta\rho g\hat{w}_0(h)$, $\hat{\tau}_{rz1}(h) = 0$, $\hat{\tau}_{zz0}^\Delta(0) - \rho_1 g\hat{w}_0(0) = -\hat{q}_0^*$ and $\hat{\tau}_{rz1}(0) = 0$, introducing the local incremental stress component

$$\hat{\tau}_{zz0}^\Delta = \hat{\tau}_{zz0} + \rho g\hat{w}_0 \quad (23)$$

(see Table 3). The differential equation system (in dimensional variables) for displacements and stresses within the elastic layer are

$$\frac{d\hat{u}_1}{dz} - k\hat{w}_0 - \frac{1}{\mu^e} \hat{\tau}_{rz1} = 0, \quad (24a)$$

$$\frac{d\hat{w}_0}{dz} + k\hat{u}_1 = 0, \quad (24b)$$

$$\frac{d\hat{\tau}_{rz1}}{dz} - 4\mu^e k^2 \hat{u}_1 - \rho_1 g k \hat{w}_0 - k\hat{\tau}_{zz0}^\Delta = 0, \quad (24c)$$

$$\rho_1 g \frac{d\hat{w}_0}{dz} + k\hat{\tau}_{rz1} + \frac{d\hat{\tau}_{zz0}^\Delta}{dz} = 0 \quad (24d)$$

for which there exists a set of analytical solutions. As shown in equations (19a) and (19b), it is necessary to construct the horizontal solutions $\hat{u}_1(k, z)$. The dimensional solution for this horizontal displacement-dependent variable in system (24a)–(24d) is

$$\begin{aligned} \hat{u}_1(k, z) = & kq \cdot \{ e^{2kz} \xi^{(-)}(k)z + e^{4hk} \xi^{(+)}(k)z \\ & - e^{2k(h+z)} \Xi^{(-)}(k, z) - e^{2hk} \Xi^{(+)}(k, z) \} / 2e^{k(2h+z)} \\ & \cdot \{ -4k^2(1 + 2h^2 k^2) \mu_1^e + g[4hk^2 \mu_1^e(\rho_1 + \delta\rho) - \rho_1 \delta\rho g] \\ & + (4k^2 \mu_1^e + g^2 \rho_1 \delta\rho) \cosh(2hk) + 2k\mu_1^e g(\rho_1 + \delta\rho) \\ & \cdot \sinh(2hk) \}, \end{aligned} \quad (25)$$

Table 3. Summary of Stress Tensor Fields

Stress Tensor	Definition
τ	perturbed GIA (Cauchy material incremental) stress ^a
τ^Δ	perturbed GIA (local incremental) stress ^b
σ^{GIA}	GIA stress with pressure of Coulomb sign convention
$\sigma^{(0)}$	tectonic stress with pressure of Coulomb sign convention

^a $\tau^{(\delta)}$ in the notation of *Wolf* [1991, 2002].

^b $\tau^{(\Delta)}$ and $\delta\tau$ in the notation of *Wolf* [1991, 2002] and IJ98, respectively.

where dimensional modified wave numbers

$$\xi^\pm(k) \equiv 2k\mu_1^e \pm g\delta\rho,$$

and parameter

$$\Xi^\pm(k, z) \equiv 2k\mu_1^e [2hk(h - z) \pm z] - g\delta\rho(2h - z)$$

are introduced. The $\hat{u}_1(k, z)$ solution is critical to retrieving the z - and r -dependent solutions for the stress components $\tau_{\theta\theta}$ and τ_{rr} as is seen in equations (19a) and (19b). After manipulation, equation (25) can be shown to be identical to the recent solution $\hat{u}_1(k, 0)$ of *O'Keefe and Wu* [2002] for the same boundary value problem.

4.2.2. Principal Stresses

[30] In reference to the orthogonal principal planes in Cartesian coordinates [*Malvern*, 1969, pp. 88–89], for individual disks the principal stresses, σ_n ($n = 1, 2, 3$), are

$$\{\sigma_n\} = \left\{ \tau_{\theta\theta}, \frac{1}{2}(\tau_{rr} + \tau_{zz}) \pm \frac{1}{2}[\tau_{rr}^2 + 4\tau_{rz}^2 - (2\tau_{rr} - \tau_{zz})\tau_{zz}]^{\frac{1}{2}} \right\}. \quad (26)$$

Rotated into the principal frame of the tectonic stress field, the new combined principal stresses of $\sigma^{GIA} + \sigma^{(0)}$ are computed. All of the Coulomb and Mogi-von Mises failure stress parameters for single disks may be derived from the above GIA stress solution information in this manner. The principal directions are computed using a formal eigenvector method [*Malvern*, 1969, p. 86] in either local or global Cartesian frames. For multiple disks, the new principal system (and tensor) may be solved for only after all contributions to the six Cartesian stress components are properly added.

5. Physics of the Disk Loading Stress

5.1. Stress Structure in the Elastic Layer

[31] The penetration of the load stress field into the elastic lithosphere is sensitive to both the spatial distribution and surface profile of the axisymmetric surface load. Figure 3 shows stress contours in 2-D cross-sectional profile in the top (elastic) layer for loads with square-edged (Figures 3a–3c) and bell-shaped (Figures 3d–3f) cross-sectional profiles. The load is emplaced at $t = 0$ and held constant thereafter with the stress field evaluated for $t \rightarrow \infty$. Both loads have axial symmetry, but for Figures 3a–3c the surface normal traction is uniform, while for Figures 3d–3f they taper off with r (also see Figure A1 of Appendix A). A 350 km radius is possibly similar to the load dimension existing in coastal south-

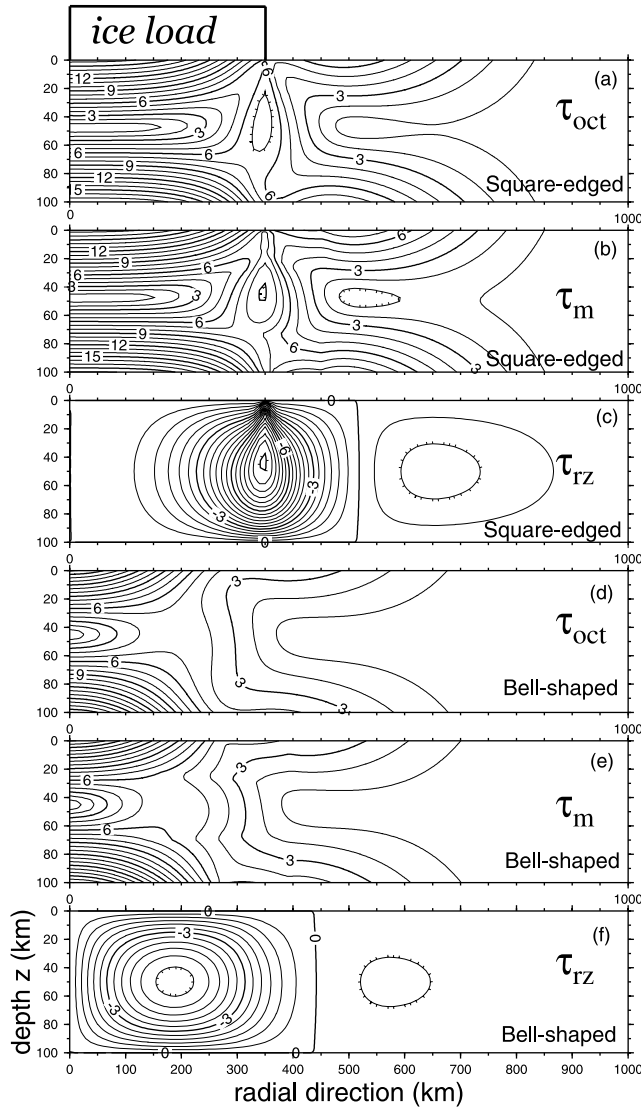


Figure 3. Cross-sectional GIA stress contours in MPa for (a)–(c) square-edged and (d)–(f) bell-shaped loads. Lithospheric thickness is $h = 100$ km, and peak load height is 1500 m. The disk radius is 350 km, and ρ_{ice} is given in Table 4, but the Earth structure densities are $\rho_1 = 2800$ and $\rho_2 = 3300 \text{ kg/m}^3$, respectively.

eastern Antarctica during the mid-Holocene [Domack *et al.*, 1991]. The center of the load has a thickness of 1.5 km for both load shapes. The two shapes used as examples in Figure 3 are end-member loading types. In the numerical studies of the northeastern Antarctic plate a series of square-edged disk loads are assumed.

[32] An interesting feature of the stress penetration profiles shown in Figure 3 is the strong change in stress that occurs just outside the lateral boundary of the load. This is especially pronounced near the surface in the uniform surface load case. In Figures 3a–3c the contours of shear stress form a tear drop shape, with the sharp edge of the tear drop occurring just at the boundary of the surface load.

[33] The Coulomb (ΔF_C) and Mogi-von Mises (ΔF_M) failure stresses are contoured in MPa in Figure 4, assuming a lithostatic (isotropic) reference state and the parameters of

Figure 3. Just below the load, a notable contrast is in the depth dependence for depths shallower than about $z \leq 5$ km. Particularly in areas of failure promotion, however, the two criteria predict broadscale features that are qualitatively similar. In the depth range of interest ($8 \leq z \leq 20$ km), where continental seismic energy release is maximum, the vertical gradients are small for both ΔF_C and ΔF_M .

[34] During the evolution of the Antarctic ice sheet the ice load drives slow viscoelastic relaxation of the mantle. Both the load evolution and the viscoelastic mantle flow tend to move such stress boundaries in space within the brittle elastic lithosphere. Since the development of the relative ability of the lithosphere to become susceptible to brittle failure is an additional complexity, it may be anticipated that the interaction of spatially and temporally realistic loading/unloading events can produce somewhat nonintuitive patterns and evolutions of relative failure stresses at depth.

5.2. Three Disk Load Test Case

[35] Figure 5 shows the predicted change in failure stress caused by the loading of three square-edged disks, each with an identical ice load history, solid Earth structure parameters (including rheology), but two differing assumptions about the failure criteria. Figure 5 maps the spatial distribution of stress response in terms of $-\Delta F$. This quantity is a measure

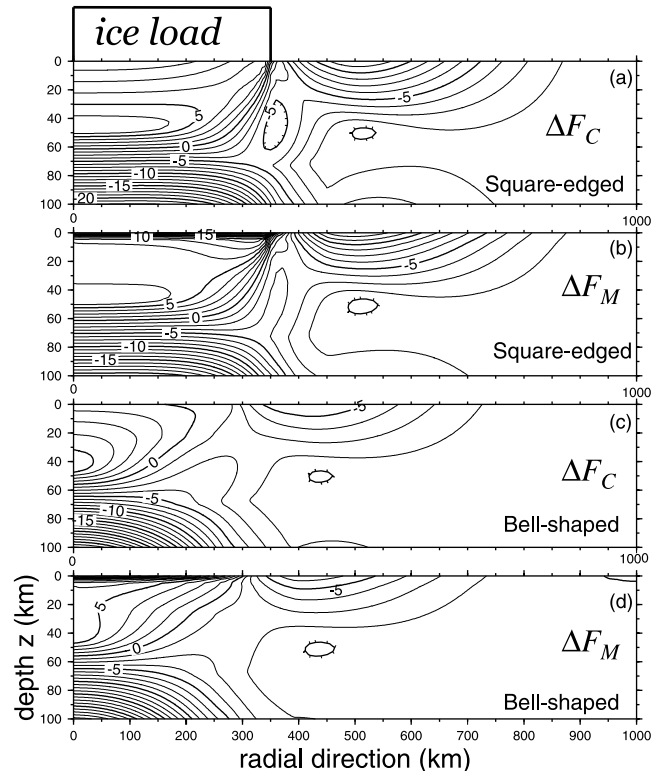


Figure 4. Contours of failure stresses for geometric load types of Figure 3. All parameters are as in Figure 3. The reference state is assumed isotropic (lithostatic). For Coulomb (ΔF_C) calculations the stress state is at the origin in τ versus σ_N space (see Figure 2a) in the reference state and hence is set to zero. Coulomb calculations assume $\mu_f = 0.7$ and Mogi-von Mises (ΔF_M) parameters of Chang and Haimson [2000] as discussed in section 3.2.

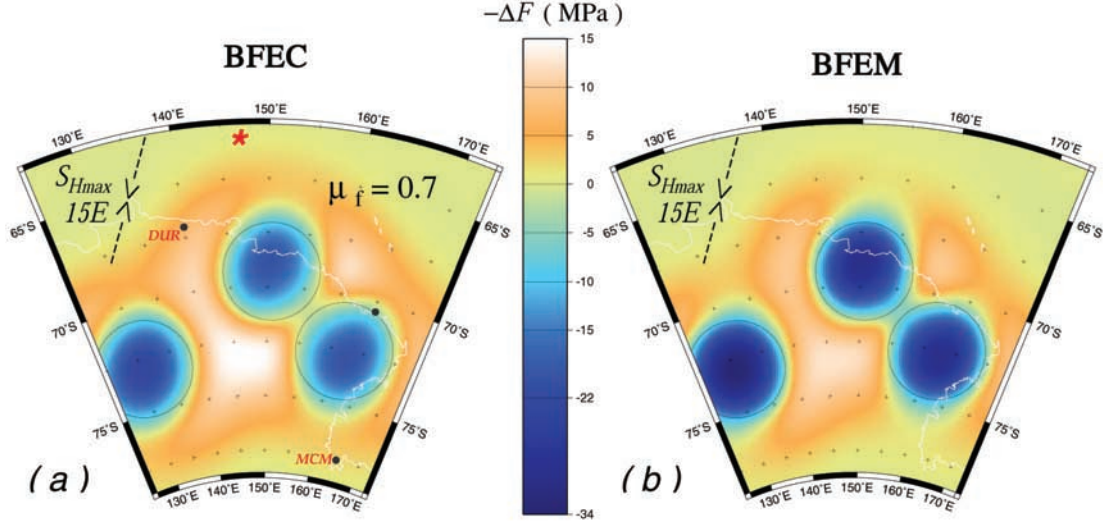


Figure 5. Present-day differential (a) Coulomb (BFEC) and (b) Mogi-von Mises (BFEM) failure stress response at 9 km depth for three square-edged disks. Each disk has a radius $\alpha = 225$ km. Higher values predict promotion of seismicity, while lower values ($-\Delta F < 0$) predict muting relative to the tectonic state. Note the anisotropy induced by the tectonic state as reflected in the stress interaction patterns. The loading in each case assumes one glacial cycle with growth to ice thicknesses of 1.5 km at the time of stress evaluation. For Figure 5a, $\mu_f = 0.7$. In both Figures 5a and 5b, $h = 80$ km, $S_{hmin}/S_{hmax} = 0.6$, and $\eta = 5.5 \times 10^{20}$ Pa s. Here, and in subsequent cases, S_V is lithostatic and condition (13) is assumed for the reference state. (See text for other parameters and Table 6 for BFEC and BFEM definitions.)

of the promotion (positive) or suppression (negative) of brittle failure, relative to the tectonic state. Each of the ice disks produce failure stress responses characterized by well-defined perimeters. The latter is due, in part, to the assumed load cross section. In both cases the load history assumes a linear growth over 85 kyr to a maximum height of 1.5 km followed by constant loading for 3 kyr, at which time the stress field is evaluated and plotted. In this way, the $-\Delta F$ maps of Figure 5 show the elastic lithospheric failure stress response in the ice loaded state. The test cases in Figure 5 assume a lithospheric thickness of $h = 80$ km and mantle viscosity $\eta = 5.5 \times 10^{20}$ Pa s. Other parameters are given in Table 4 and the depth of evaluation, z , is 9 km, approximately the depth of rupture initiation for the Balleny Island earthquake (Figure 1b). (The subscripts M and C are here, and henceforth, dropped in the notation for ΔF for discussion of the map-view comparisons.)

5.2.1. Coulomb Response at Loading Maximum

[36] An anisotropy is introduced by the initial tectonic state and this is reflected in the stress interaction patterns shown in Figure 5a. Here S_{Hmax} is oriented at $15^\circ E$ (see Figure 1) and a ratio $S_{hmin}/S_{Hmax} = 0.95$ is assumed. Note that failure tends to be inhibited along an axis, relative to each of the circular disks, at about $15^\circ E$. Figure 5a predicts regions of intense earthquake promotion, with $-\Delta F \approx 10$ – 15 MPa. However, these regions are, in part, a result of the model assumption of square-edged disks which increase the predicted shear at the load margins as shown in Figure 3. Each load disk generates paired lobes of enhanced susceptibility to failure that align with the direction of horizontal tectonic stress S_{Hmax} .

5.2.2. Mogi-Von Mises Response at Loading Maximum

[37] Mogi-von Mises failure criteria is considered in Figure 5b. The BFEM stress patterns in 5b are quite similar

to the patterns and amplitudes predicted in frame a for BFEC. Deep within the ice disk interiors seismicity is suppressed at a $-\Delta F < -15 \sim -30$ MPa level. It is important to keep in mind that this criteria uses the space τ_{oct} versus σ_m for defining brittle failure instability. Subtle differences in the stress shadowing shown in Figure 5, however, suggest that the role played by the failure criteria when assuming a realistic load history does merit further study. This is the main motivation of the section that follows.

6. Predictions of Present-Day ΔF in George V Land and Environs

6.1. Load History

[38] *James and Ivins* [1998] interpreted a glacial maximum reconstruction of *Denton et al.* [1991] to compute estimates of the Antarctic GIA geodetic signature. This model, originally termed *D91*, has subsequently been updated for the Bellinghausen Sea, the Antarctic Peninsula

Table 4. Model Solid Earth Mechanical Parameters^a

Symbol	Definition	Model Value
ρ_{ice}	ice density	917.4 kg m^{-3}
ρ_1	lithospheric density	2800 kg m^{-3}
ρ_2	mantle (half-space) density	5511 kg m^{-3}
g	uniform gravity	9.8322 m s^{-2}
μ_1^e	lithospheric rigidity	31.5 GPa
μ_2^e	mantle (half-space) rigidity	44.5 GPa
η	mantle (half-space) viscosity	variable
h	lithospheric thickness	variable

^aFigures 5–7 and Figure A1 assume $\rho_2 = 3300 \text{ kg m}^{-3}$, and for Figures 8–10, assume $\mu_2^e = 97.7$ GPa.

Table 5. Ice Load Thicknesses (Meters) Among Recent Deglaciation Models

Dome C 125°E, 74.95°S			Edmondson Pt. (See Maps)			Dumont d'Urville DUR (See Maps)			Wilkes Basin at 150°E, 70°S		
A0	ANT5a ^a	D91-1.5	A0	ANT5a ^a	D91-1.5	A0	ANT5a ^a	D91-1.5	A0	ANT5a ^a	D91-1.5
~50	100	294	175	250	732	50	500	666	500	500	1011
						16 kyr BP					
~75	20	89	150	50	244	50	100	222	150	100	337
						7 kyr BP					

^aLGM heights are taken identical to the 12 kyr values of *Nakada et al.* [2000]. (See section 6.1 of text for discussion.)

and the western Weddell Sea by *Ivins et al.* [2000, 2002] and tuned to the timing of retreat estimated by *Denton and Hughes* [2000], *Goodwin and Zweck* [2000], and *Hall et al.* [2001]. The latest update is termed *D91-1.5* [*Ivins et al.*, 2001] and is assumed for the brittle failure analysis reported here. The primary features of *D91-1.5* include (1) a reduction of the total mass exchange with the ocean from 24.5 (*D91*) to 12.5 m of eustatic sea level rise equivalent (SLE) and (2) a lengthening of the deglaciation period, with initiation at 22 kyr BP and termination at 2–0 kyr BP.

[39] The modeled deglaciation from 22 to 11 kyr BP is smaller in the continental interior than in *D91*. For the Ross Embayment sector and easternmost East Antarctica, ≈ 2.08 m and 4.17 m SLE remain at 11 kyr BP, respectively. Thereafter, the pace of deglaciation increases and by 8 kyr the modeled mass loss of these two regions reduces the remaining SLE to 1.03 m and 2.15 m, respectively. At 6 kyr BP the remaining SLE is 1.27 m for the combined regions. Minor late Holocene change occurs along the coast, similar to the model of *Huybrechts* [2002]. Other features of *D91-1.5* glacial loading are discussed in Appendix B.

[40] Since the relevant viscosity range is assumed to be above 4×10^{20} Pa s, the details of the collapse between 5 and 0 kyr BP are found to be relatively unimportant to the present-day stress predictions. The load history includes two prior 100 kyr glacial cycles. No ocean loading is included. The predicted lithospheric stress shadowing, consequently, is that solely caused by Antarctic continental glacial isostasy.

6.2. Other Load Considerations

[41] The *D91-1.5* model is similar to the *ANT5a* model of *Nakada et al.* [2000] and the *A0* model of *Huybrechts* [2002] in both the timing and magnitude of coastal loading. A brief summary of some important quantitative differences among the three models is given in Table 5 for locations relevant to the present study. The George V Land and Terre Adelie (see Figure 1b) coastal load is adjusted in *D91-1.5* to coincide with the mid-Holocene ice grounded near the Mertz-Ninnis and Dumont d'Urville Troughs (i.e., near DRV in Figure 1b) [*Domack et al.*, 1991]. The load includes a feature quite like the coastal ice dome near 113°E, 66.5°S advocated by *Goodwin and Zweck* [2000]. The recent *A0* model simulation by *Huybrechts* [2002] also

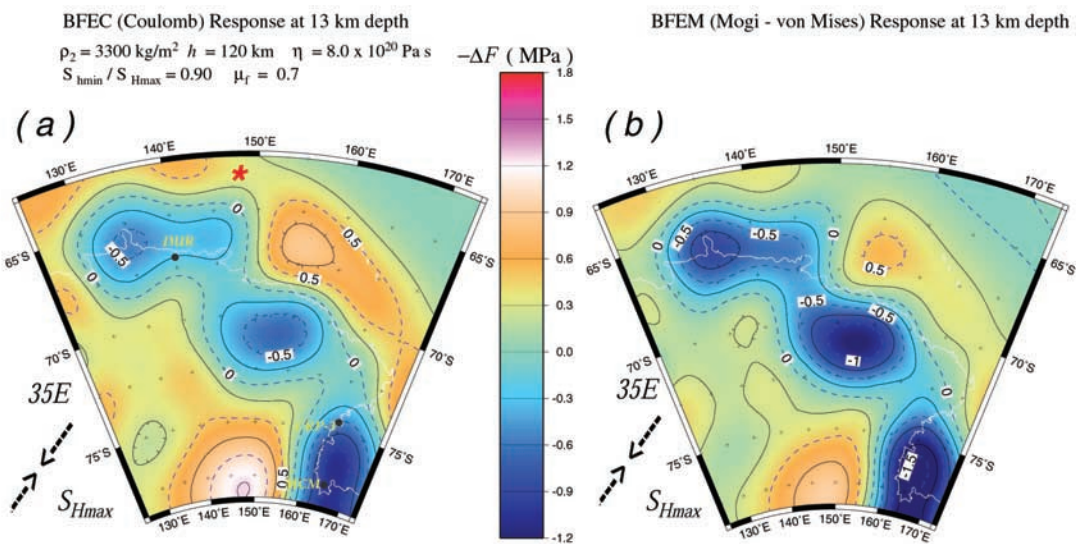


Figure 6. Present-day differential (a) Coulomb (BFEC) and (b) Mogi-von Mises (BFEM) failure stress responses at 13 km depth computed for the *D91-1.5* ice load model with three glacial cycles. Note the robust magnitudes and the similarity of the two predictions for $-\Delta F$.

Table 6. Initial Stress States for Numerical Parameter Study

State	Definition
BFEC	below frictional equilibrium - Coulomb criteria
BFEM	below frictional equilibrium - Mogi—von Mises criteria

features coastal George V Land geometrical complexity in the loading/unloading history. Since the timing of *ANT5a* and *A0* are similar to *D91-1.5* the average thickness ratios (Table 5) may be used to roughly rescale the failure stress predictions for these alternative ice models.

6.3. Predicted Patterns of Present-Day $-\Delta F$

[42] The illustrative maps of Figure 5 show the anisotropic behavior of the predicted failure patterns and provide

an estimate of the magnitude of GIA stresses that nudge the Archean crust of East Antarctica closer to, or further from, brittle failure. Both the antiquity and tectonics of this region [Goodge and Fanning, 1999; Dalziel and Lawver, 2001] are consistent with the assumption of an initial stress that is below frictional equilibrium.

[43] For a depth of 13 km Figure 6 shows the predicted present-day BFEC and BFEM stresses (Table 6) assuming the *D91-1.5* ice history (section 6.1). The assumed lithospheric thickness ($h = 120$ km) is identical to that assumed in both the *D91* predictions of Antarctic crustal motion [James and Ivins, 1998] and in the global model computations for ICE-3G [Tushingham and Peltier, 1991]. This value of h and the value for mantle viscosity, $\eta = 8.0 \times 10^{20}$ Pa s for Figure 6, are within a factor of

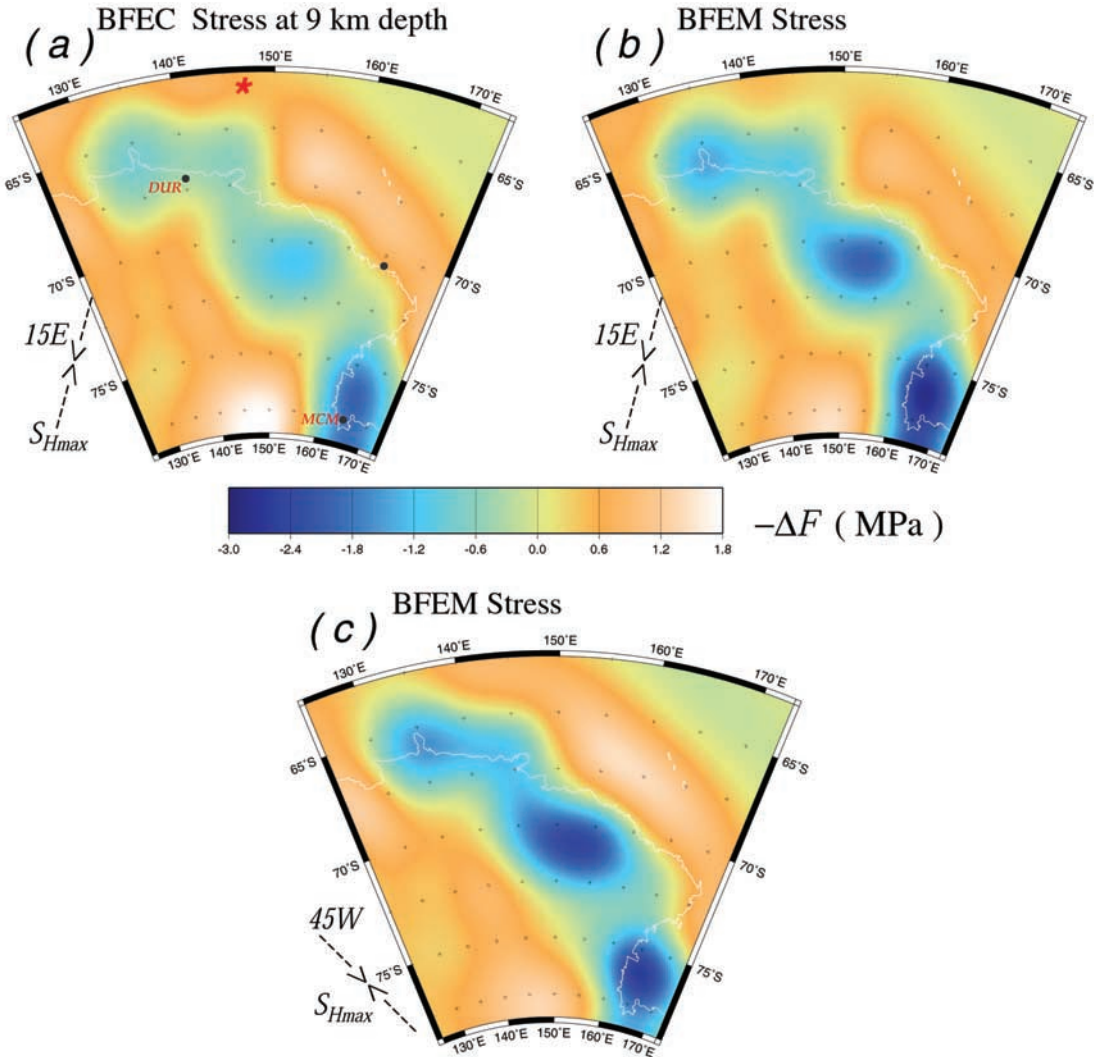


Figure 7. Present-day differential (a) Coulomb (BFEC) and (b)–(c) Mogi-von Mises (BFEM) stress patterns. All cases assume Earth structure of Table 4 except $\rho_2 = 3300$ kg/m³. Additionally, $\eta = 1.0 \times 10^{21}$ Pa s, $h = 120$ km, and $S_{hmin}/S_{Hmax} = 0.95$, and Figure 7a assumes $\mu_f = 0.7$. Figure 7c assumes a tectonic S_{Hmax} rotated counterclockwise by 60° from the orientation of N15°E of Figures 7a and 7b. Deglaciation is the same as is assumed in Figure 6 with tectonic stresses and strength parameters as indicated. The red star at the center-top of the map view in Figure 7a is the approximate position of the 25 March 1998 (M_w 8.1) Balleny Island earthquake.

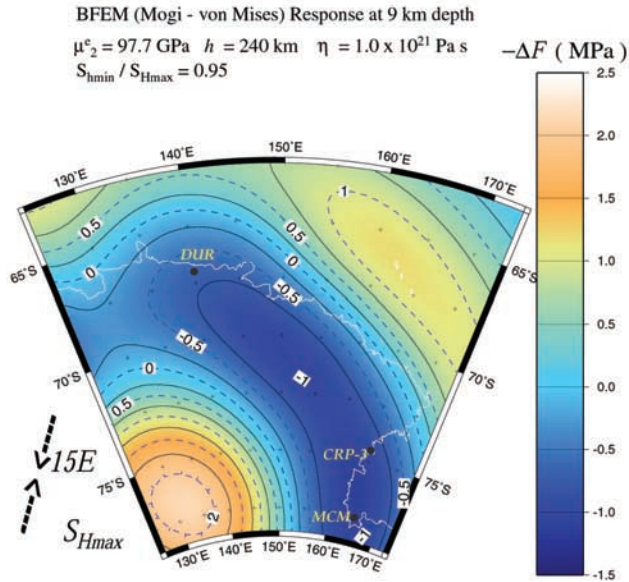


Figure 8. Present-day differential Mogi-von Mises (BFEM) failure stress response with thick 240 km lithosphere using the same load history as in Figures 6 and 7.

0.7–1.3 of the viscosity models that successfully characterize GIA processes in northern Europe [Lambeck, 1997; Davis *et al.*, 1999; Milne *et al.*, 2001; Peltier *et al.*, 2002]. The calculations assume a tectonic stress orientation of N35°E, consistent with the great Antarctic plate earthquake (Figure 1b).

[44] The predicted pattern of $-\Delta F$ in Figure 6 is complex, reflecting contributions from load size, timing and disk load pattern. As in the test load case of Figure 5, contours of $-\Delta F$ are somewhat stretched in the direction

of S_{Hmax} (N35°E) and show quantitative predictions that are at a similar level and of similar pattern for the two criteria. Peak stresses for BFEC seismicity promotion are roughly 1.5 times those of BFEM predictions, while seismicity diminution is larger by about a factor of 2 for BFEM. The juxtaposition of failure enhancement in the Wilkes Basin with the failure suppression in the Ross Sea east of the Transantarctic Mountains owes to complex spatiotemporal interactions between adjacent loading and unloading model elements.

6.3.1. Tectonic S_{Hmax} at N15°E

[45] We now consider variations in the orientation of S_{Hmax} since this is so poorly constrained in the region. Stress maps for the same load history and lithospheric thickness are shown in Figure 7 as assumed in Figure 6. Here, however, the assumed S_{Hmax} direction is rotated counterclockwise 20°. Although in Figures 7a and 7b the stretched contours of $-\Delta F$ rotate approximately 20° counterclockwise, the overall effect is small and has little influence on the promoted failure zones. The changes in assumed mantle viscosity (8×10^{20} versus 10×10^{20}) and depth of evaluation (13 versus 9 km) between the computations in Figures 6, 7a, and 7b, respectively, are of minor consequence to these predictions and comparisons (also see section 5.1 and Figure 4).

6.3.2. Tectonic S_{Hmax} at N45°W

[46] In situ measurements of principal stresses using induced fracturing at the Cape Roberts drill site (CRP-3) have recently been reported by Jarrard *et al.* [2001]. While the drill fracture data indicate that a background stress system given by equation (13) is plausible, the orientation of S_{Hmax} may be quite different than assumed in the computations for Figures 6a, 6b, 7a, and 7b (N35°E and N15°E, respectively). The N35°E orientation is consistent with the intraplate earthquake rupture solutions of Tsuboi *et al.* [2000], Antolik *et al.* [2000], and Henry *et al.* [2000]. In contrast, the CRP-3 data indicate

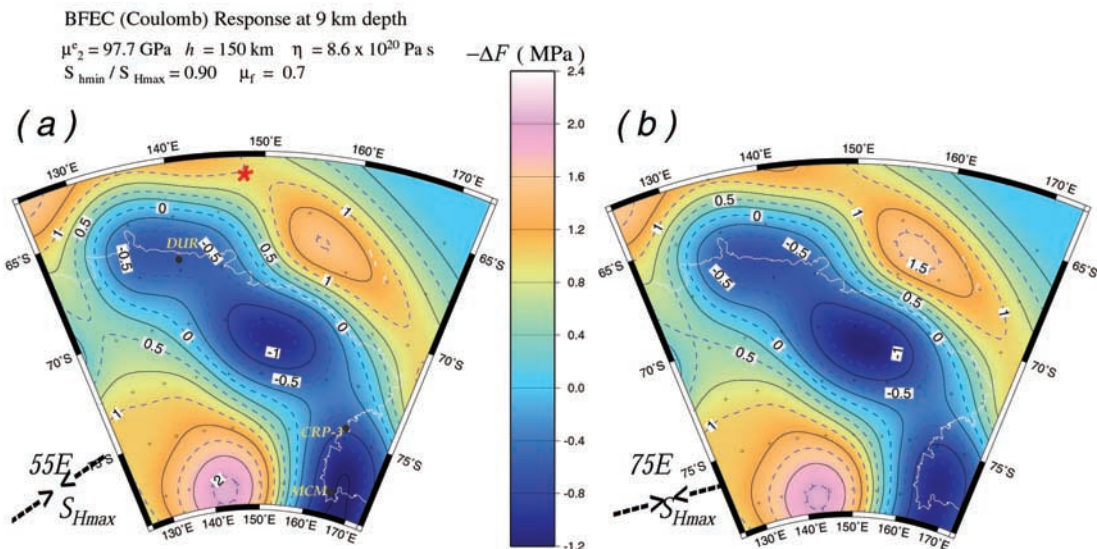


Figure 9. Present-day Coulomb (BFEC) failure stress pattern for S_{Hmax} at (a) 55° and (b) 75°E. The half-space viscosity is $\eta = 8.6 \times 10^{20} \text{ Pa s}$, and the thickness of the lithosphere is $h = 150 \text{ km}$, intermediate between Figures 6 and 7 (120 km) and Figure 8 (240 km).

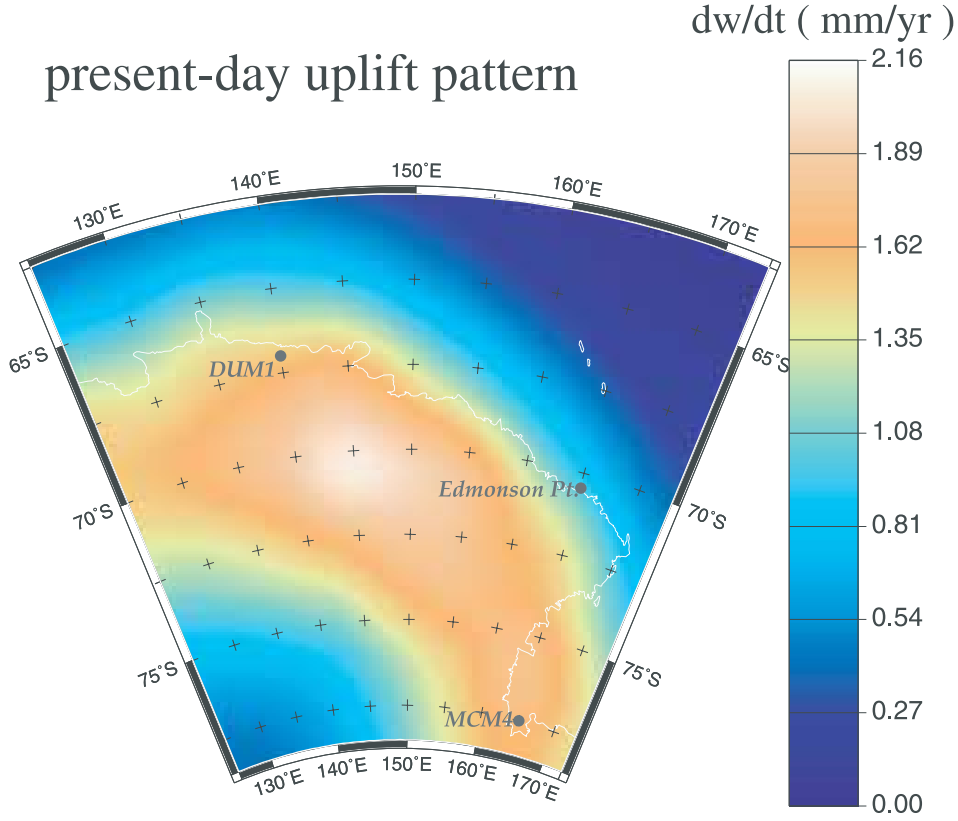


Figure 10. Present-day surface vertical motion assuming parameters of Figure 9. The map prediction illustrates the local scale of present-day vertical crustal isostasy associated with the failure stress maps of this paper. The positions of the Dumont d'Urville (DUM1) and McMurdo (MCM4) permanent GPS tracking stations are also indicated.

a N45°W direction for S_{Hmax} ; a 80° counterclockwise rotation with respect to the N35°E orientation assumed for the computational results in Figure 6. The predicted patterns of $-\Delta F$ in Figure 7c (with S_{Hmax} at N45°W and the BFEM failure condition) are broadly similar to Figures 7a and 7b. With the N45°W orientation, however, the undulations of the boundaries between promotion and suppression zones are smaller and this underscores the importance of the tectonic stress orientation in predicting the detailed pattern of present-day GIA-induced seismicity. *Wu et al.* [1999] also found a strong sensitivity of rebound failure stress predictions to the tectonic background field.

6.4. Predictions for Thick Cratonic Lithosphere

[47] In Figure 8 the same initial tectonic stress orientation as assumed in Figure 6 is used with a mantle viscosity of 1.0×10^{21} , but now with a lithospheric thickness of 240 km, double that assumed in Figures 6 and 7. A value of $h = 240$ km is an appropriate upper bound for the East Antarctic craton [*Danesi and Morelli*, 2000; *Fredericksen et al.*, 2001] since typical modeled thicknesses of the thermal lithosphere exceed those of the corresponding mechanical lithosphere [*Pasquale et al.*, 2001]. For a 240 km thick lithosphere, BFEM and BFEC predictions are similar in pattern and magnitude hence only the BFEM case is shown in Figure 8. The long wavelength features of

the stress pattern are quite robust at a lithospheric thickness value of $h = 240$ km.

[48] In Figure 9 BFEC predictions of $-\Delta F$ are shown for $h = 150$ km with assumed tectonic stress orientations of N55°E and N75°E. Here a viscosity is assumed that is the preferred value determined in a recent analysis by *Milne et al.* [2001] for Fennoscandia ($\eta = 8.6 \times 10^{20}$ Pa s). The lithospheric thickness ($h = 150$ km) is within the acceptable range determined by *Milne et al.* [2001] for Fennoscandian rebound models of GPS crustal motion data. Here long-wavelength features are also promoted, though not as strongly as in the $h = 240$ km case shown in Figure 8. As in Figure 8, two regions in Figure 9 show the promotion of Coulomb failure stress to the level of 1 to 2 MPa, one within the continental interior in Wilkes Basin and one located several hundred km offshore (shifting slightly to the east or west depending on the assumed orientation of S_{Hmax}). The pattern is akin to surface bulge migration during postglacial rebound [*Wu and Peltier*, 1982] and the change of sign is seen in other models of failure stress after deglaciation [*Klemann and Wolf*, 1998; *Wu et al.*, 1999].

[49] A thick East Antarctic mechanical lithosphere, of order 150–240 km, predicts substantial lateral penetration of failure stress. In fact, it penetrates several hundreds of km offshore into the northeastern sector of the Antarctic plate and GIA processes may therefore be partially responsible

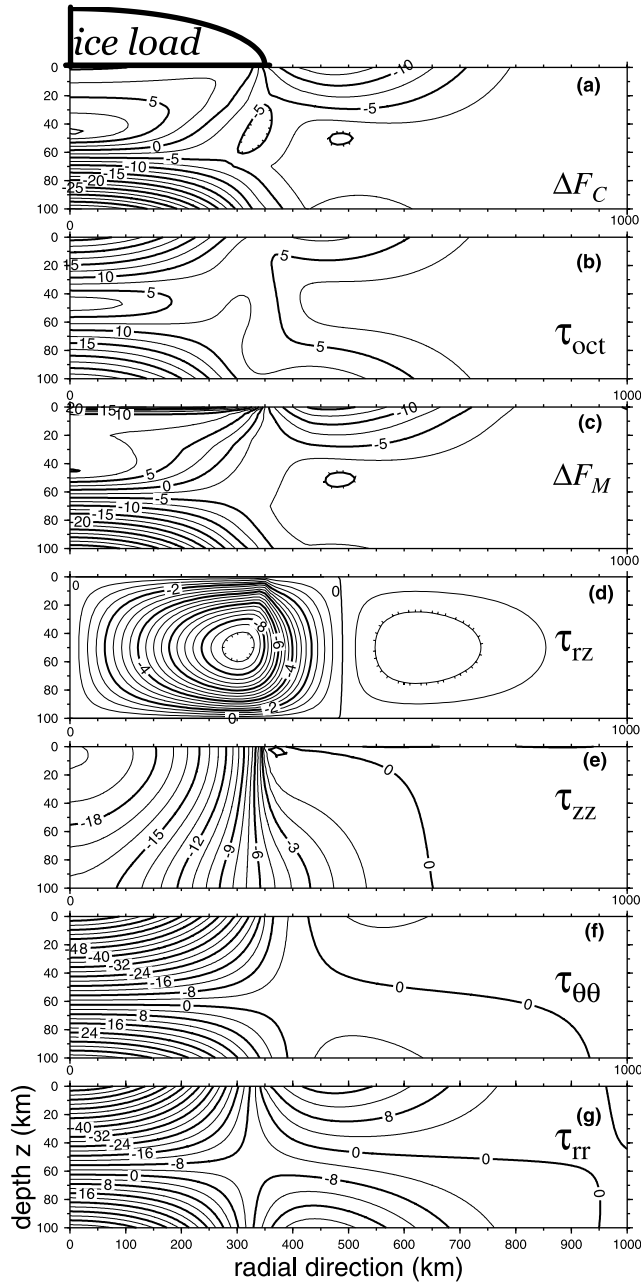


Figure A1. Contours of GIA stress components in 2-D profile (in MPa) in the top elastic layer ($h = 100$ km). An elliptically shaped surface load profile is assumed with $t \rightarrow \infty$ and $\alpha = 350$ km. Also plotted are the failure stresses ΔF_C and ΔF_M with isotropic reference state as in Figure 4 with the same failure law parameters. Height at disk center is 2.25 km, and the densities are as in Figures 3 and 4. Plots of τ_{rr} , $\tau_{\theta\theta}$, and τ_{zz} with $\alpha = 333$ km match those of *Johnston et al.* [1998] for the same Earth structure parameters and peaked parabola.

for triggering the 25 March 1998 M_w 8.1 Balleny Island earthquake as suggested by *Tsuboi et al.* [2000] and *Kreemer and Holt* [2000]. A 120 km thick lithosphere allows for such triggering, but less ubiquitously so, as exemplified in the stress map of Figure 6b.

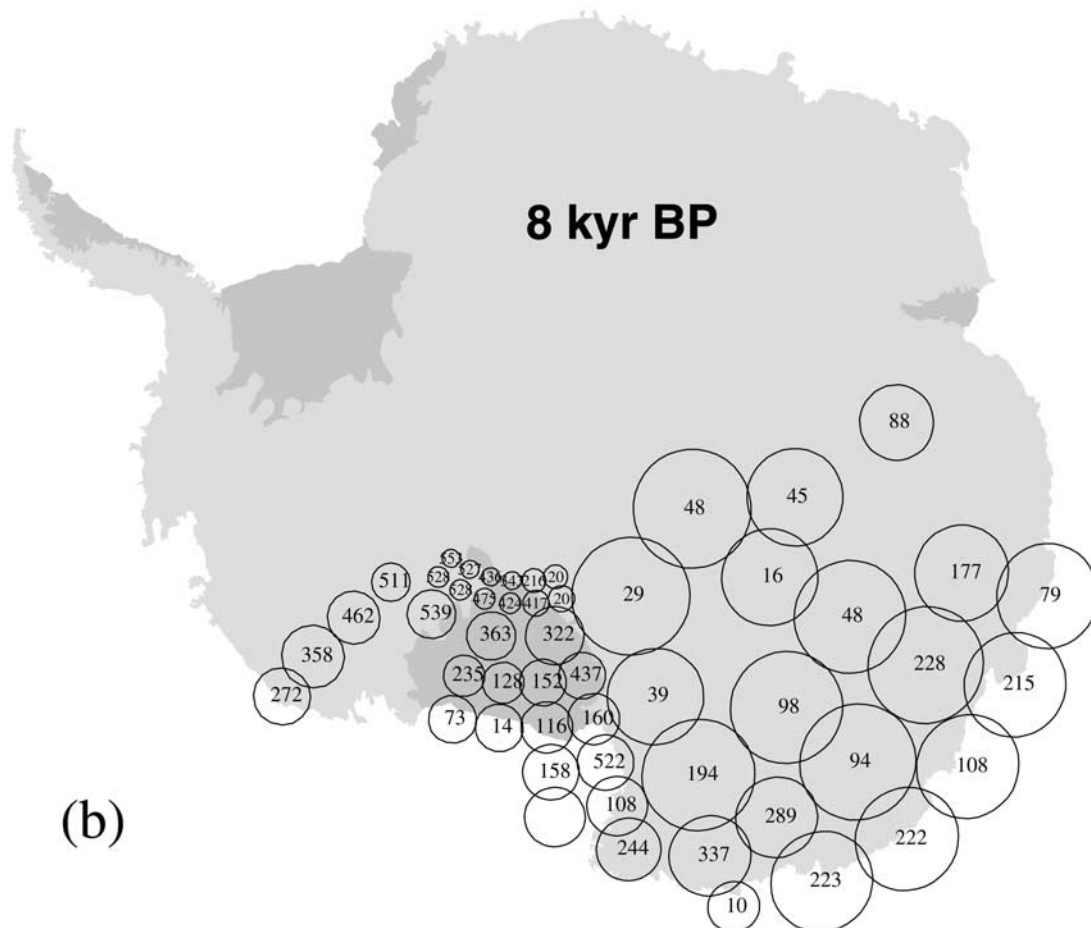
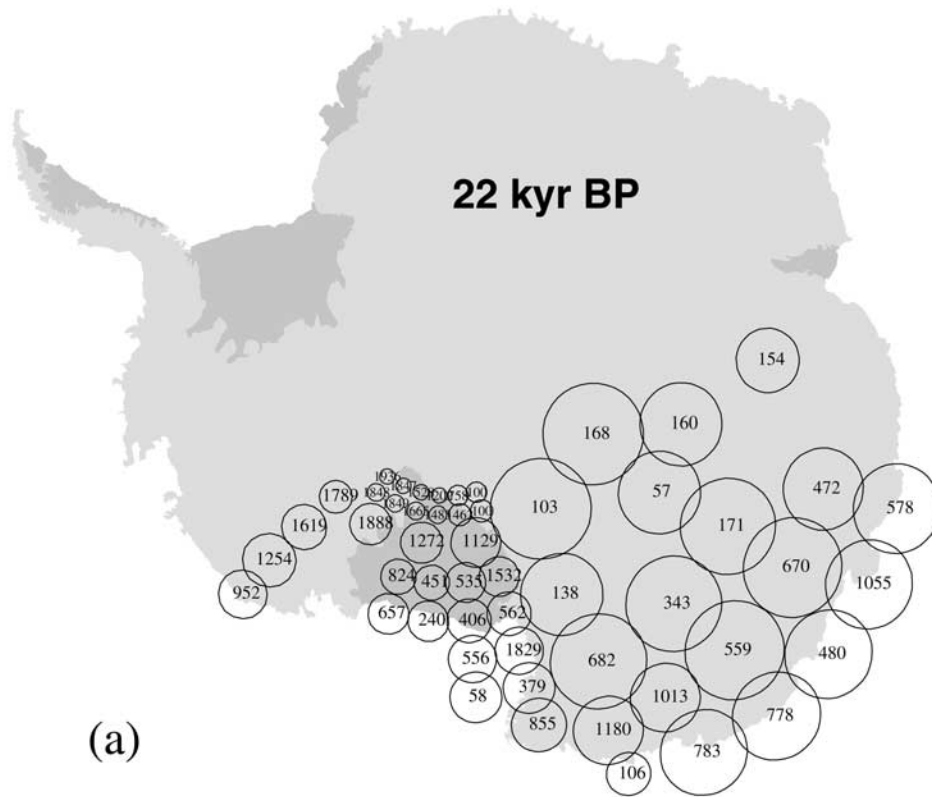
[50] The predicted uplift rate is shown in Figure 10 assuming the Earth structure used for computing brittle failure stresses in Figure 9. The uplift pattern is also broadscale, but is unaffected by the anisotropy associated with background tectonic stresses. A similar regional broad pattern of uplift is computed assuming a stratified mantle and thinner lithosphere with the *D91-1.5* load terminating at 2 kyr BP by *Ivins et al.* [2001]. The stress patterns tend to align with the gradients in the uplift pattern and not necessarily with the locus of maximum uplift rate. This is a feature *Hicks et al.* [2000] recently noted in the earthquake patterns of northern coastal Norway.

6.5. Discussion and Future Directions

[51] A shortcoming of the simplified theoretical computations of failure stresses presented here is the absence of layering in the mantle. If a lower mantle were included that has a substantially higher viscosity than the upper mantle then larger stresses would be maintained in the modeled brittle crust. This role of the lower mantle viscosity, with its potential for a one order-of-magnitude increase over the value assigned to the upper mantle, was first discussed by *Spada et al.* [1991]. It is of note that the Coulomb stresses calculated by *Wu et al.* [1999], with a $20\times$ more viscous lower than upper mantle, are more robust than those calculated here, considering the more youthful unloading involved for Antarctica. *Klemann and Wolf* [1998, 1999] also demonstrate that stratification within the crust, lithosphere and shallow mantle have important influences on GIA stress relaxation processes in the upper crust. Future models of Antarctic rebound stresses should also consider the role of such stratification. Unlike Fennoscandia and eastern Canada, however, virtually no data currently constrain models of viscous stratification in the Antarctic region.

[52] The modeling employed here also makes the simplifying incompressibility assumption, and *Wu et al.* [1999] have shown that compressibility may enhance the peak estimates of $|\Delta F|$ by as much as 30–65%. Although compressibility and viscous stratification are important considerations, the uncertain tectonic stress orientation, the poorly constrained load history and the influence of strong contrasts in mechanical strength at depth across the Transantarctic Mountain Ranges [*Ritzwoller et al.*, 2001; *Danesi and Morelli*, 2001] are added factors that must weigh upon future strategies for computing forward model GIA brittle failure stresses in the Antarctic plate environment.

Figure B1. (opposite) *D91-1.5* ice heights in meters for the study region and surrounding areas at (a) 22 kyr, (b) 8 kyr, and (c) 5 kyr BP. Computations of geoid change and crustal uplift rates are presented for the complete *D91-1.5* ice model by *Ivins et al.* [2001].



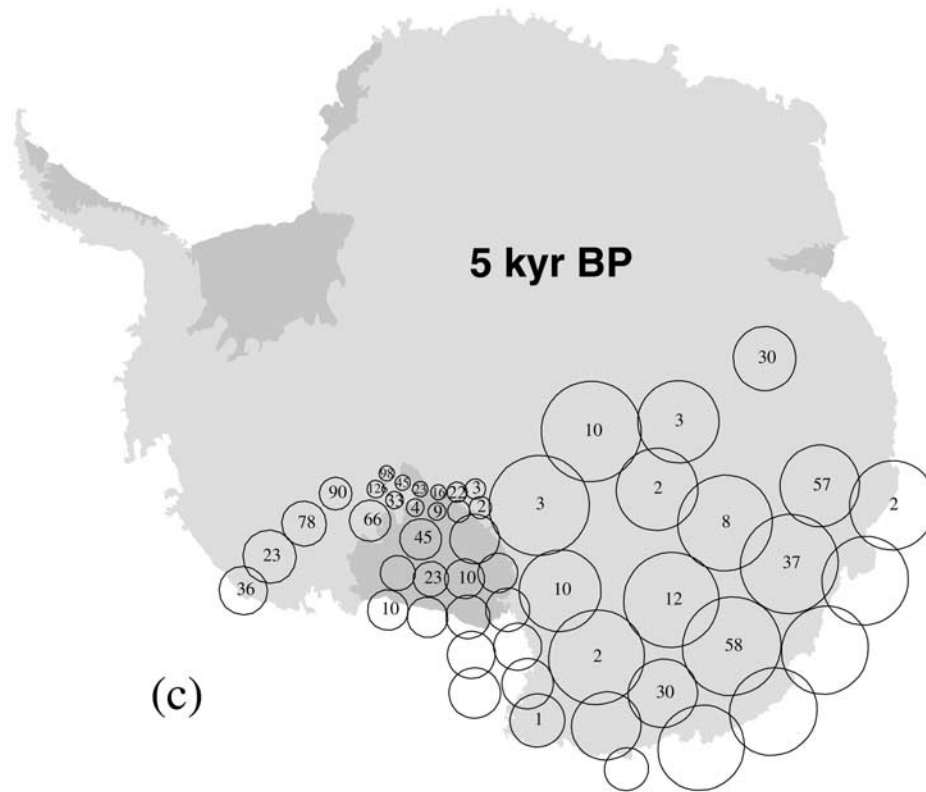


Figure B1. (continued)

[53] The relative timing and magnitude of deglaciation also influence GIA driven seismicity. This aspect of the stress predictions will improve as constraints on the glacial history tighten in the future. Certain features of the models presented, like the contrast in predicted seismicity across the Transantarctic Mountain Ranges between the Ross Embayment and Wilkes Basin, are sensitive to the glacial history and such details need to be tested using improved load models. Ultimately, seismicity observations could provide an important way to test models of ongoing rebound in the region.

7. Summary and Conclusions

[54] Lithospheric thickness has a strong influence on the predicted patterns of postglacial seismicity. *Johnston et al.* [1998] also noted the importance of this parameter in modeling GIA seismicity and faulting in northern Europe. The surface wave tomographic mapping by *Danesi and Morelli* [2001] and *Ritzwoller et al.* [2001] reveal a deep seated high-velocity anomaly beneath the crust of East Antarctica, indicating that a thick elastic lithosphere exists there. The anomaly extends 200–500 km northwest of Wilkes Land beneath oceanic crust. The crust and uppermost mantle in East Antarctica are associated with one of the most ancient of Earth's cratons [*Dalziel*, 1991; *Borg and DePaolo*, 1994]. Thermo-petrologic models for the mechanical structure of Archean cratonic continental lithosphere favor a thickness $h \geq 150$ km [*Rudnick et al.*, 1998; *Jaupart and Mareschal*, 1999].

[55] If GIA-induced stresses brought the crust to failure at the site of the great intraplate earthquake of 25 March 1998 (M_w 8.1), some 320 km offshore, the penetration length scale must be large. Such a strong lateral penetration of the GIA failure stresses is promoted by a thick lithosphere. Similarly, *Grollmund and Zoback* [2000] interpret the stress profile deduced from deep well pore pressure changes as reflective of a postglacial flexure, implying that the GIA stresses presently extend some 200 km offshore from the former Fennoscandian ice sheet in southwestern Norway. The tectonic stress levels in our numerical models are large with $S_{Hmax} - S_{Hmin} \approx 25$ MPa, which is about equal to the estimated stress drop on the main Balleny Islands subevent of 25 March 1998 [*Henry et al.*, 2000]. Consequently, GIA acts only as a triggering mechanism if it is, indeed, the cause of this strike slip event. Postglacial loading is a viable mechanism for triggering strike slip rupturing outside of the loaded region [*Wu and Hasegawa*, 1996a] especially for favorable preexisting tectonic states [*Schultz and Zuber*, 1994].

[56] We have computed the stress tensor evolution in the lithosphere with semianalytic techniques for viscoelastic Earth models [*Ivins and James*, 1999; *Thoma and Wolf*, 1999; *Ivins et al.*, 2000, 2002] and applied differential Coulomb and Mogi-von Mises fracture criteria to the prediction of seismic failure. Although the numerical values of ΔF differ to within a factor of 1.5–2, the similarity of the Coulomb and Mogi-von Mises stresses (compare panels a and b of Figures 5, 6, and 7) shows that predictions of fracture susceptibility are rather insensitive to the assumed

failure law. This gives additional credence therefore to GIA stress results which have previously relied solely on Coulomb analyses.

[57] Our numerical results reveal the importance of improving the constraints on the regional tectonic stress. While tectonic stress may be reasonably reconstructed from the compound rupture interpretation of the Balleny Island earthquake [Henry *et al.*, 2000; Antolik *et al.*, 2000], the Neogene continental faulting patterns [Wilson, 1999] or from the global mantle-lithospheric flow models of Steinberger *et al.* [2001], new crustal borehole stress data from the western Ross Sea [Jarrard *et al.*, 2001] indicate a quite different orientation for S_{Hmax} . It is possible that the tectonic stress field is spatially heterogeneous across the vast extent of the northeastern Antarctic plate. Nevertheless, our modeling strongly suggests that the Antarctic crust should be seismically active because of GIA processes, regardless of the details of the tectonic stress state.

Appendix A: Load Shape

[58] As discussed in section 5.1 and 5.2 concern must be given to the assumed model cross-sectional shape of the cylindrically symmetric load. Calculations with elliptical cross-section load types is also provided here. Figure A1 shows stress contours in 2-D profile in the top elastic layer for an elliptically shaped surface load profile at $t \rightarrow \infty$ and $\alpha = 350$ km. Included are the failure stresses predicted by BFEC (ΔF_C) and BFEM (ΔF_M) assumptions (with lithostatic reference state), the octahedral stress (τ_{oct}) and the 4 incremental stress components. These may be directly compared to contours plotted for the response to square-edged and bell-shaped type disk loading shown in Figures 3 and 4. The total volume of the ice load is identical to the square-edged case of Figure 3. Note the differences between τ_{rz} and that of a square-edged disk in Figure 3c. Note, again, the promotion of the failure stresses just outside the loaded area. Generally, however, the dimension of the load versus the lithospheric thickness is also an important consideration. This sensitivity has been the subject of recent studies by Klemann and Wolf [1998] and Johnston *et al.* [1998]. Although the shapes are important when considering shallow fracturing close to the load margin, the differences between brittle failure predictions among full deglaciation simulations is small (~ 10 – 30%) at depths where seismic energy released in the crust is greatest ($8 < z < 20$ km).

Appendix B: Load History

[59] For the purposes of computing the brittle failure stress responses our initial computational simulations included the full refined disk structures of *D91-1.5*. However, via iteration, the number of disks was reduced by a factor of 3 to enhance computational efficiency. The square edged disks that are used for computing Wilkes Land lithospheric response in the Antarctic plate are shown in Figure B1 at 22, 8, and 5 kyr BP (frames a, b, and c, respectively). Approximations are the inclusion of the Ross Sea ice load and a ridge of ice disks along the 135°E longitude from about 85°S to the Marie Byrd Land Coast. The ridge is a far field

load approximation, having a total mass equivalent to about 353 Tt ($1 \text{ Tt} = 10^{15} \text{ kg}$ with 360 Tt corresponding to an ice mass sufficient to change global sea level by 1 meter). Within the region of interest (Figure 1b) Last Glacial Maximum (LGM) is simulated using a coarse disk representation. The Ross sector at LGM has an ice load mass of 903 Tt ($\approx 2.5 \text{ m}$ of SLE). Throughout northern Victoria Land, and for all loads to the west of the Transantarctic Mountain Range and east of 90°E (see Figure 1), the LGM load is 1,890 Tt (or $\approx 5.25 \text{ m}$ SLE).

[60] Modeled deglaciation from 22 to 11 kyr BP is of moderate size in the continental interior, similar to the recent Huybrechts [2002] model. The Ross Embayment sector and easternmost East Antarctic maintain $\approx 2.08 \text{ m}$ and 4.17 m SLE respectively, at 11 kyr BP, after which ablation is more rapid. By 8 kyr BP the modeled ice loss of the two respective regions reduces the SLE values to 1.03 m and 2.15 m, and by 6 kyr BP the deglaciation model has a remaining SLE 0.14, 0.33 and 0.8 m of mass load equivalent for the 135°E ridge, the Ross sector and East Antarctica, respectively. The *D91-1.5* ice history continues collapsing and is almost complete by 5 kyr BP. Minor late Holocene ice change occurs along the coastal disks. Deglaciation in the model occurs up to AD 1500, and not thereafter. The continent-wide *D91-1.5* model has average negative mass balance over the last 5 kyr BP that is well below 0.1 mm/yr SLE [Ivins *et al.*, 2001].

[61] **Acknowledgments.** This work was performed by Jet Propulsion Laboratory, California Institute of Technology, under contract with NASA (ERI), by Pacific Geoscience Centre, an office of the Geological Survey of Canada (TJS) and by the SEAL project, German Federal Ministry of Education and Research (BMBF) Project SF2000/13 (VK). The authors wish to acknowledge important communications with Bruce Banerdt, Stephan Bannister, Stefania Danesi, Shamita Das, Andrea Donnellan, Masaki Kanao, Paul Lundgren, Carol Raymond, Michael Ritzwoller, Seiji Tsuboi and Terry Wilson. Generic Mapping Tools (GMT) software [Wessel and Smith, 1991] produced many of the figures presented in this paper. Constructive reviews by Allison Bent, Ctirad Matyska, Giorgio Spada, and Detlef Wolf are greatly appreciated. Grants from the Solid Earth and Natural Hazards Program of NASA's Earth Science Office provided the support for this research. Geological Survey of Canada Contribution 2002195.

References

- Adams, J., Postglacial faulting in eastern Canada: Nature, origin and seismic hazard implications, *Tectonophysics*, 163, 323–331, 1989.
- Antolik, M., A. Kaverina, and D. S. Dreger, Compound rupture of the great 1998 Antarctic plate earthquake, *J. Geophys. Res.*, 105, 23,825–23,838, 2000.
- Arvidsson, R., Fennoscandian earthquakes: Whole crustal rupturing related to postglacial rebound, *Science*, 274, 744–746, 1996.
- Bannister, S., and B. N. L. Kennett, Seismic activity in the Transantarctic Mountains—Results from a broadband array deployment, *Terra Antarct.*, 9, 41–46, 2002.
- Borg, S. G., and D. J. DePaolo, Laurentia, Australia and Antarctica as a Late Proterozoic supercontinent, *Geology*, 22, 307–310, 1994.
- Brady, M., M. D. Zoback, K. Fuchs, F. Rummel, and J. Baumgärtner, Estimation of the complete stress tensor to 8 km depth in the KTB scientific drill holes: Implications for crustal strength, *J. Geophys. Res.*, 102, 18,453–18,475, 1997.
- Candie, S. C., J. M. Stock, R. D. Müller, and T. Ishihara, Cenozoic motion between East and West Antarctica, *Nature*, 404, 145–150, 2000.
- Chang, C., and B. Haimson, True triaxial strength and deformability of the German Continental Deep Drilling Program (KTB) deep hole amphibolite, *J. Geophys. Res.*, 105, 18,999–19,013, 2000.
- Dalziel, I. W. D., Pacific margins of Laurentia and East Antarctica—Australia as a conjugate rift pair: Evidence and implications for an Eo-Cambrian supercontinent, *Geology*, 19, 598–601, 1991.
- Dalziel, I. W. D., and L. A. Lawver, The lithospheric setting of the West Antarctic ice sheet, in *The West Antarctic Ice Sheet: Behavior and*

- Environment, Antarctic Res. Ser.*, vol. 77, edited by R. B. Alley and R. A. Bindshadler, pp. 29–44, AGU, Washington, D. C., 2001.
- Danesi, S., and A. Morelli, Group velocity of Rayleigh waves in the Antarctic region, *Phys. Earth Planet. Int.*, 122, 55–66, 2000.
- Danesi, S., and A. Morelli, Structure of the upper mantle under the Antarctic Plate from surface wave tomography, *Geophys. Res. Lett.*, 28, 4395–4398, 2001.
- Davis, J. L., J. X. Mitrovica, H.-G. Scherneck, and H. Fan, Investigations of Fennoscandian glacial isostatic adjustment using modern sea level records, *J. Geophys. Res.*, 104, 2733–2747, 1999.
- Dehls, J. F., O. Olesen, L. Olesen, and L. Harald-Blikra, Neotectonic faulting in northern Norway: The Storgurra and Nordmannvikdalen postglacial faults, *Quat. Sci. Rev.*, 19, 1447–1460, 2000.
- Denton, G. H., and T. J. Hughes, Reconstruction of the Ross ice drainage system, Antarctica, at the Last Glacial Maximum, *Geogr. Ann., Part A*, 82, 143–166, 2000.
- Denton, G. H., M. L. Prentice, and L. H. Burckle, Cainozoic history of the Antarctic ice sheet, in *Geology of Antarctica*, edited by R. J. Tingey, pp. 365–433, Oxford Univ. Press, New York, 1991.
- Dietrich, R., et al., ITRF coordinates and plate velocities from repeated GPS campaigns in Antarctica—An analysis based on different individual solutions, *J. Geod.*, 74, 756–766, 2001.
- Domack, E. W., A. J. T. Jull, and S. Nakao, Advance of East Antarctic outlet glaciers during the Hypsithermal: Implications for the volume state of the Antarctic ice sheet under global warming, *Geology*, 19, 1059–1062, 1991.
- Engelder, T., *Stress Regimes in the Lithosphere*, 459 pp., Princeton Univ. Press, Princeton, N. J., 1992.
- Fredericksen, A. W., M. G. Bostock, and J. F. Cassidy, S-wave velocity structure of the Canadian lithosphere, *Phys. Earth Planet. Int.*, 124, 175–191, 2001.
- Gambino, S., and E. Privitera, Characterization of earthquakes recorded by Mt. Melbourne volcano seismic network (northern Victoria Land, Antarctica), *Terra Antarct.*, 1, 167–172, 1994.
- Goodge, J. W., and C. M. Fanning, 2.5 b.y. of punctuated Earth history as recorded in a single rock, *Geology*, 27, 1007–1010, 1999.
- Goodwin, I. D., and C. Zweck, Glacio-isostasy and glacial ice load at Law Dome, Wilkes Land, East Antarctica, *Quat. Res.*, 53, 285–293, 2000.
- Grollmund, B., and M. D. Zoback, Post glacial lithospheric flexure and induced stresses and pore pressure changes in the northern North Sea, *Tectonophysics*, 327, 61–81, 2000.
- Hall, B. L., G. H. Denton, and B. Overturf, Glacial Lake Wright, a high-level Antarctic lake during the LGM and early Holocene, *Antarct. Sci.*, 13, 53–60, 2001.
- Hasegawa, H. S., Neotectonics and inferred movements in Canada, *Bull. Geol. Surv. Finl.*, 60, 3–25, 1988.
- Henry, C., S. Das, and J. H. Woodhouse, The great March 25, 1998, Antarctic Plate earthquake: Moment tensor and rupture history, *J. Geophys. Res.*, 105, 16,097–16,118, 2000.
- Hicks, E. C., H. Bungmar, and C. D. Lindholm, Seismic activity, inferred crustal stresses and seismotectonics in the Rana region, northern Norway, *Quat. Sci. Rev.*, 19, 1423–1436, 2000.
- Hill, D. P., Contemporary block tectonics: California and Nevada, *J. Geophys. Res.*, 87, 5433–5450, 1982.
- Hori, T., and Y. Kaneda, Morgan Hill earthquake in the stress shadow of the 1906 San Francisco earthquake, *Geophys. Res. Lett.*, 28, 2261–2264, 1991.
- Huybrechts, P., Sea-level changes at the LGM from ice-dynamic reconstructions of the Greenland and Antarctic ice sheets during the glacial cycles, *Quat. Sci. Rev.*, 21, 203–231, 2002.
- Ivins, E. R., and T. S. James, Simple models for late Holocene and present-day Patagonian glacier fluctuations and predictions of a geodetically detectable isostatic response, *Geophys. J. Int.*, 138, 601–625, 1999.
- Ivins, E. R., T. H. Dixon, and M. P. Golombek, Extensional reactivation of an abandoned thrust: A bound on shallowing in the brittle regime, *J. Struct. Geol.*, 12, 303–314, 1990.
- Ivins, E. R., C. A. Raymond, and T. S. James, The influence of 5000 year-old and younger glacial mass variability on present-day rebound in the Antarctic Peninsula, *Earth Planets Space*, 52, 1023–1029, 2000.
- Ivins, E. R., X. Wu, C. A. Raymond, C. F. Yoder, and T. S. James, Temporal geoid of a rebounding Antarctica and potential measurement by the GRACE and GOCE satellites, in *I. A. G. Symposia 123: Gravity, Geoid and Geodynamics 2000*, edited by M. G. Sideris, pp. 361–366, Springer-Verlag, New York, 2001.
- Ivins, E. R., C. A. Raymond, and T. S. James, Late-Pleistocene, Holocene and present-day ice load evolution in the Antarctic Peninsula: Models and predicted vertical crustal motion, in *Ice Sheets, Sea Level and the Dynamic Earth*, *Geodyn. Ser.*, vol. 29, edited by J. X. Mitrovica and B. L. A. Vermeersen, pp. 133–154, AGU, Washington, D. C., 2002.
- Jaeger, J. C., *Elasticity, Fracture and Flow With Engineering and Geological Applications*, 268 pp., Chapman and Hall, New York, 1969.
- James, T. S., and A. L. Bent, A comparison of eastern North American seismic strain-rates to glacial rebound strain-rates, *Geophys. Res. Lett.*, 19, 2127–2130, 1994.
- James, T. S., and E. R. Ivins, Predictions of Antarctic crustal motions driven by present-day ice sheet evolution and by isostatic memory of the Last Glacial Maximum, *J. Geophys. Res.*, 103, 4993–5017, 1998.
- Jarrard, R. D., D. Moos, T. J. Wilson, C. J. Bucker, and T. S. Paulsen, Stress patterns observed by borehole televiewer logging of the CRP-3 drillhole, Victoria Land Basin, Antarctica, *Terra Antarct.*, 8, 203–211, 2001.
- Jaupart, C., and J. C. Mareschal, The thermal structure and thickness of continental roots, *Lithos*, 48, 93–114, 1999.
- Johnston, A. C., The effect of large ice sheets on earthquake genesis, in *Earthquakes at North American Passive Margins: Neotectonics and Postglacial Rebound*, *NATO ASI Ser., Ser. C*, vol. 266, edited by S. Gregersen and P. W. Basham, pp. 581–599, Springer-Verlag, New York, 1989.
- Johnston, P., P. Wu, and K. Lambeck, Dependence of horizontal stress magnitude on load dimension in glacial rebound models, *Geophys. J. Int.*, 132, 41–60, 1998.
- Jones, S., Late Quaternary faulting and neotectonics, south Victoria Land, Antarctica, *J. Geol. Soc. London*, 154, 645–652, 1996.
- Kanamori, H., and E. E. Brodsky, The physics of earthquakes, *Phys. Today*, 102, 34–40, 2001.
- King, G. C. P., R. S. Stein, and J. Lin, Static stress changes and the triggering of earthquakes, *Bull. Seismol. Soc. Am.*, 84, 935–953, 1994.
- Klemann, V., and D. Wolf, Modelling of stresses in the Fennoscandian lithosphere induced by Pleistocene glaciations, *Tectonophysics*, 294, 291–303, 1998.
- Klemann, V., and D. Wolf, Implications of a ductile layer for the deformation caused by the Fennoscandian ice sheet, *Geophys. J. Int.*, 139, 216–226, 1999.
- Kreemer, C., and W. E. Holt, What caused the March 25, 1998 Antarctic plate earthquake?: Inferences from regional stress and strain rate fields, *Geophys. Res. Lett.*, 27, 2297–2300, 2000.
- Kuge, K., M. Kikuchi, and Y. Yamanaka, Non-double-couple moment tensor of the March 25, 1998 Antarctic earthquake: Composite rupture of strike-slip and normal faults, *Geophys. Res. Lett.*, 26, 3401–3404, 1999.
- Lagerbäck, R., Neotectonic structures in northern Sweden, *Geol. Foeren. Stockholm Foerh.*, 100, 263–269, 1979.
- Lagerbäck, R., Dating of late Quaternary faulting in northern Sweden, *J. Geol. Soc. London*, 149, 285–292, 1992.
- Lambeck, K., Sea-level changes along the French Atlantic and channel coasts since the time of the Last Glacial Maximum, *Palaeogeogr. Palaeoclimatol. Palaeoecol.*, 129, 1–22, 1997.
- Malvern, L. E., *Introduction to the Mechanics of a Solid Medium*, 713 pp., Prentice-Hall, Old Tappan, N. J., 1969.
- Milne, G. A., J. L. Davis, J. X. Mitrovica, H. G. Scherneck, J. M. Johansson, M. Vermeer, and H. Koivula, Space-geodetic constraints on glacial isostatic adjustment in Fennoscandia, *Science*, 291, 2381–2385, 2001.
- Mogi, K., Fracture and flow of rocks under high triaxial compression, *J. Geophys. Res.*, 76, 1255–1269, 1971.
- Morein, G., D. L. Turcotte, and A. Gabrielov, On the statistical mechanics of distributed seismicity, *Geophys. J. Int.*, 131, 552–558, 1997.
- Muir-Wood, R., Extraordinary deglaciation reverse faulting in northern Fennoscandia, in *Earthquakes at North American Passive Margins: Neotectonics and Postglacial Rebound*, *NATO ASI Ser., Ser. C*, vol. 266, edited by S. Gregersen and P. W. Basham, pp. 141–174, Springer-Verlag, New York, 1989.
- Nakada, M., R. Kimura, J. Okuno, K. Moriwaki, H. Miura, and H. Mae-moku, Late Pleistocene and Holocene melting history of the Antarctic ice sheet derived from relative sea-level variations, *Mar. Geol.*, 167, 85–103, 2000.
- O'Keefe, K., and P. Wu, Effect of mantle structure on postglacial induced horizontal displacement, in *Ice Sheets, Sea Level and the Dynamic Earth*, *Geodyn. Ser.*, vol. 29, edited by J. X. Mitrovica and B. L. A. Vermeersen, pp. 109–118, AGU, Washington, D. C., 2002.
- Pasquale, V., M. Verdoya, and P. Chiozzi, Heat flux and seismicity in the Fennoscandian Shield, *Phys. Earth Planet. Int.*, 126, 147–162, 2001.
- Peltier, W. R., I. Shennan, R. Drummond, and B. Horton, On the postglacial isostatic adjustment of the British Isles and the shallow viscoelastic structure of the Earth, *Geophys. J. Int.*, 148, 443–475, 2002.
- Pondrelli, S., and R. Azzara, Upper mantle anisotropy in Victoria Land (Antarctica), *Pure Appl. Geophys.*, 151, 433–442, 1998.
- Reading, A. M., Antarctic seismicity and neotectonics, in *Antarctica at the Close of a Millennium*, *Proc. 8th International Symposium on Antarctic Earth Science*, Wellington, N. Z., July, 1999, edited by J. A. Gamble, D. N. B. Skinner, and S. Henrys, *Bull. R. Soc. N. Z.*, 35, 479–484, 2002.

- Ritzwoller, M. H., N. M. Shapiro, A. L. Levshin, and G. M. Leahy, Crustal and upper mantle structure beneath Antarctica and surrounding oceans, *J. Geophys. Res.*, **106**, 30,645–30,670, 2001.
- Roult, G., J.-P. Montagner, E. Stutzmann, S. Barbier, and G. Guiveneux, The GEOSCOPE program: Its data center, *Phys. Earth Planet. Int.*, **113**, 25–43, 1999.
- Rudnick, R. L., W. F. McDonough, and R. J. O'Connell, Thermal structure, thickness and composition of continental lithosphere, *Chem. Geol.*, **145**, 395–411, 1998.
- Salvini, F., G. Brancolini, M. Buseti, F. Storti, F. Mazzarini, and F. Coren, Cenozoic geodynamics of the Ross Sea region, Antarctica: Crustal extension, intraplate strike-slip faulting, and tectonic inheritance, *J. Geophys. Res.*, **102**, 24,669–24,696, 1997.
- Schultz, R. A., and M. T. Zuber, Observations, models and mechanisms of failure of surface rocks surrounding planetary surface loads, *J. Geophys. Res.*, **99**, 14,691–14,702, 1994.
- Sneddon, I. H., *The Use of Integral Transforms*, 539 pp., McGraw-Hill, New York, 1972.
- Spada, G., D. A. Yuen, R. Sabadini, and E. Boschi, Lower mantle viscosity constrained by seismicity around deglaciated regions, *Nature*, **351**, 53–55, 1991.
- Stein, R. S., The role of stress transfer in earthquake occurrence, *Nature*, **402**, 605–609, 1999.
- Steinberger, B., H. Schmeling, and G. Marquart, Large-scale lithospheric stress field and topography induced by global mantle circulation, *Earth Planet. Sci. Lett.*, **186**, 75–91, 2001.
- Storti, F., F. Rossetti, and F. Salvini, Structural architecture and displacement accommodation mechanisms at the termination of the Priestley Fault, northern Victoria Land, Antarctica, *Tectonophysics*, **341**, 141–161, 2001.
- Sugden, D. E., M. A. Summerfield, G. H. Denton, T. I. Wilch, W. C. McIntosh, D. R. Marchant, and R. H. Rutherford, Landscape development in the Royal Society Range, southern Victoria Land, Antarctica: Stability since the mid-Miocene, *Geomorphology*, **28**, 181–200, 1999.
- Summerfield, M. A., F. M. Stuart, H. A. P. Cockburn, D. E. Sugden, G. H. Denton, T. Dunai, and D. R. Marchant, Long-term rates of denudation in the Dry Valleys, Transantarctic Mountains, southern Victoria Land, Antarctica based on in-situ-produced cosmogenic ^{21}Ne , *Geomorphology*, **27**, 113–129, 1999.
- Thoma, M., and D. Wolf, Bestimmung der Mantelviskosität aus Beobachtungen der Landhebung und Schwere in Fennoskandien, *GFZ Potsdam Sci. Tech. Rep. STR99/02*, 101 pp., GeoForschungsZentrum, Potsdam, Germany, 1999.
- Tsuboi, S., M. Kikuchi, Y. Yamanaka, and M. Kanao, The March 25, 1998 Antarctic earthquake: Great earthquake caused by postglacial rebound, *Earth Planets Space*, **52**, 133–136, 1998.
- Tushingham, A. M., and W. R. Peltier, ICE-3G: A new global model of late Pleistocene deglaciation based upon geophysical predictions of post-glacial relative sea-level, *J. Geophys. Res.*, **96**, 4497–4523, 1991.
- Van der Wateren, F. M., and S. A. P. L. Cloetingh, Feedbacks of the lithosphere dynamics and environmental change of the Cenozoic West Antarctic rift system, *Global Planet. Change*, **23**, 1–24, 1999.
- Wessel, P., and W. H. F. Smith, Free software helps map and display data, *Eos Trans. AGU*, **72**, 65–81, 1991.
- Wilson, T. J., Cenozoic transtension along the Transantarctic Mountains–West Antarctic rift boundary, southern Victoria Land, Antarctica, *Tectonics*, **14**, 531–545, 1995.
- Wilson, T. J., Cenozoic structural segmentation of the Transantarctic Mountains rift flank in southern Victoria Land, *Global Planet. Change*, **23**, 105–127, 1999.
- Wolf, D., The normal modes of a layered, incompressible Maxwell half-space, *J. Geophys.*, **57**, 106–117, 1985.
- Wolf, D., Viscoelastodynamics of a stratified, compressible planet, incremental field equations and short- and long-time asymptotes, *Geophys. J. Int.*, **104**, 401–417, 1991.
- Wolf, D., Gravitational viscoelastodynamics, *Acta Geod. Geophys. Hung.*, **37**, 29–60, 2002.
- Wu, P., and H. S. Hasegawa, Induced stresses and fault potential in eastern Canada due to a disc load: A preliminary analysis, *Geophys. J. Int.*, **125**, 415–430, 1996a.
- Wu, P., and H. S. Hasegawa, Induced stresses and fault potential in eastern Canada due to a realistic load: A preliminary analysis, *Geophys. J. Int.*, **127**, 215–229, 1996b.
- Wu, P., and P. Johnston, Can deglaciation trigger earthquakes in N. America?, *Geophys. Res. Lett.*, **27**, 1323–1326, 2000.
- Wu, P., and W. R. Peltier, Viscous gravitational relaxation, *Geophys. J. R. Astron. Soc.*, **70**, 435–485, 1982.
- Wu, P., P. Johnston, and K. Lambeck, Postglacial rebound and fault instability in Fennoscandia, *Geophys. J. Int.*, **139**, 657–670, 1999.
- Zoback, M. D., and B. Grollmund, Impact of deglaciation on present-day intraplate seismicity in eastern North America and western Europe, *C. R. Acad. Sci., Ser. IIa Sci. Terre Planetes*, **333**, 23–33, 2001.
- Zoback, M. L., and World Stress Map and Lithosphere Program Team Members, Global patterns of tectonic stress, *Nature*, **341**, 291–298, 1989.
- Zwartz, D., M. Bird, J. Stone, and K. Lambeck, Holocene sea-level change and ice-sheet history in the Vestfold Hills, East Antarctica, *Earth Planet. Sci. Lett.*, **155**, 131–145, 1998.

E. R. Ivins, Jet Propulsion Laboratory, California Institute of Technology, 4800 Oak Grove Drive, MS 300/233, Pasadena, CA 91109, USA. (eri@fryxell.jpl.nasa.gov)

T. S. James, Geological Survey of Canada, Sidney, B. C., Canada V8L 4B2.

V. Klemann, GFZ Potsdam, Geodesy and Remote Sensing, Telegrafenberg, D-14473 Potsdam, Germany.